UC Santa Barbara

UC Santa Barbara Electronic Theses and Dissertations

Title

Organoids to Organisms: Engineering 3D Microenvironments to Support Biological Systems

Permalink

https://escholarship.org/uc/item/2d1605m6

Author

Rosas, Jonah Mathew

Publication Date

2024

Peer reviewed|Thesis/dissertation

eScholarship.org Powered by the California Digital Library
University of California

UNIVERSITY OF CALIFORNIA

Santa Barbara

Organoids to Organisms: Engineering 3D Microenvironments to Support Biological Systems

A dissertation submitted in partial satisfaction of the

requirements for the degree

Doctor of Philosophy in Biochemistry and Molecular Biology

by

Jonah Mathew Rosas

Committee in charge:

Professor Angela A. Pitenis, Co-Chair

Professor Denise J. Montell, Co-Chair

Professor Meghan A. Morrissey

Professor Ryan S. Stowers

Professor Beth L. Pruitt

September 2024

The dissertation of Jonah Mathew Rosas is approved.

_____

Meghan A. Morrissey

_____

Ryan S. Stowers

_____

Beth L. Pruitt

_____

Angela A. Pitenis, Committee Co-Chair

_____

Denise J. Montell, Committee Co-Chair

September 2024

Organoids to Organisms: Engineering 3D Microenvironments to Support Biological Systems

Copyright © 2024

By

Jonah Mathew Rosas

To my Mom, Lisa, and Brother, Justin:

You traveled this journey alongside me. This triumph is as much yours as it is mine.

Con querida.

Acknowledgements

I will look back fondly on my time. at the University of California, Santa Barbara. The relationships I built along the way will stay with me forever. It was through generous collaboration and selfless mentorship that my work was made possible.

I must start by thanking my family, mentors, and friends who walked this journey with me.

Mom: my academic journey was filled with sacrifices – sacrifices you made so that I could follow my dream. I am forever grateful for your love, compassion, and support. This is our success.

To my brother, Justin: thank you for never letting me forget how far we've come. In the challenging times of graduate school, your words recentered me and kept me fortified. You listened to my doubts and helped me see clearly as the mist rose.

To the grandparents Antonio and Antonia Rosas: I carry you with me in my heart, and your sacrifice made this success possible. You left a family and home behind for a better life. Without your courage, I would not be here today. I am a product of the hard work and dedication you both instilled in our family.

Thank you to my undergraduate and master's research mentors: Dr. Denis Wirtz and Dr. Jamie Spangler. My early years in your labs at Johns Hopkins sparked my passion for microscopy, structural biology, and especially cancer. It took years for me to feel confident as a scientist, and the challenge and opportunities you gave me in the lab helped make me the scientist I am today.

To my doctoral advisors: Dr. Angela Pitenis and Dr. Denise Montell. Thank you both for trusting me to lead a research area in a vastly new direction. You challenged

the way I approached problems and taught me that science takes time and leads us down unexpected roads. Most of all, you supported (almost) every crazy idea I threw out there and helped me build them into a clear scientific narrative. You taught me how to lead a team and execute a research program that challenges paradigms in the field with a focus on addressing a central and tangible question. With your support, I presented my work at countless conferences nationally and received numerous awards. Thank you especially for the workspace with the ocean views!

To my thesis committee members Dr. Meghan Morrissey, Dr. Ryan Stowers, and Dr. Beth Pruitt: It has been a privilege to learn from and collaborate with each of you. You each came with such deep scientific expertise an enthusiasm that helped me enrich my doctoral experience. Your guidance ensured my research remained focused, and you generously provided your time, resources, and experimental insights.

Dr. Patrick Krohl: You taught me a great deal about who I wanted to be as a mentor. You showed me how to lead with enthusiasm, a pet parrot, and an eye for what makes people excited.

Dr. Gabriella Russo: You taught me how to believe in myself. You reminded me that mistakes were part of science. Thank you for putting your trust in me and for being a continual mentor.

Dr. Paul Kuhn: My fellow Gaucho and Blue Jay. Your mentorship both academically and professionally made a step into the industry sector less daunting. I look forward to years of constructive dialogue, debate, and most likely, disagreement.

To the past and present members of the Interfacial Engineering Lab and Denise Montell Lab: Over the last few years, you all have given me countless creative experimental next-steps and freely shared protocols, critiqued with kindness, and built my scientific confidences. There was never a dull day in the labs with all of you.

Dr. Allison Chau: We started this journey together, and now, it seems almost poetic that we conclude it together. I could not have asked for a more compassionate and organize lab mate and life-long friend. Your keen eye for illustration, communication, and mentorship pushed me to be a better scientist. I could not have asked for a better partner to have built the lab.

Dixon Atkins: It has been a true honor to watch you grow as a scientist over the past few years. From meeting you at recruitment, to seeing you dive you're your independent research. It feels like yesterday you were rotating with me in the lab. I'll cherish our constant debates.

Andrew (Anderson) Rhode: I hope you always have a good weekend. Your friendship and inquisitive scientific eye challenged me to deeply think about every aspect of my system, and your humor filled the years with levity.

Lisa Månsson: You taught me a great deal about balance. Thank you for reminding me to always make time for a little mid-day coffee break and a bike ride.

Ahmed Al Kindi: Your humor lightens every lab meeting, and I look forward to seeing the exciting scientific journey ahead of you.

Kathryn Shaffer: Thank you for taking up the mantle of “most organized person in the lab”. It was never going to be me! You have such a bright scientific future ahead, and I look forward to all you accomplish.

Dr. Joseph Campanale: We took a step into the scientific unknown together, and, I dare say, it paid off! It was no small task to start an entirely new model system, and I am glad to have done it with you. I am so excited to see how you take the findings of our work and build them out over a long and successful academic career with your own lab!

Dr. Morgan Mutch: You truly inspired me to never allow someone else’s journey of graduate school shape my own. You modeled what exceptional science was without compromising what brought you joy. Thank you for the lessons and always being ready to go get a tasty treat.

Melanie Rodriguez: It’s rare to make a friend and collaborator as incredible as you. One of my fondest graduate school memories was working on establishing our co-culture system! Thank you for years of friendship, laughter in the tissue culture room, and a keen scientific eye. I have no doubts of many years of collaboration to come.

Jacob Harwood: Your work as a part of the organoid team was truly essential. You have an efficient scientific mindset and always identify the most essential experiments. It was a privilege to work with you, mentor you in the ways of organoids, and request Matrigel® to be thawed.

Nora Wolcott and Alexa Pettitt: Thank you for your friendship, perspective, and compassion. Your friendship made graduate school a gift. I cannot wait to visit you in Boston!

Dr. Duncan Proctor: Thank. You for always listening, for reminding me I can accomplish great things, and for all the hikes. You reminded me to never take myself too seriously.

Vita Of Jonah Mathew Rosas

May 2024

EDUCATION

UNIVERSITY OF CALIFORNIA, SANTA BARBARA (Santa Barbara, CA)
Ph.D. Biomolecular Science and Engineering 2019-2024
Advisor(s): Dr. Angela A. Pitenis & Dr. Denise J. Montell
University of California Santa Barbara

JOHNS HOPKINS UNIVERSITY (Baltimore, MD)
M.S.E. Chemical and Biomolecular Engineering 2018-2019
Advisor: Dr. Jamie Spangler
Thesis: Improved Next-Generation Therapeutic Delivery Systems Through Allosteric Exchange and Selective Glycosylation

B.S. Chemical and Biomolecular Engineering 2014-2018
Emphasis: Molecular and Cellular Bioengineering

RESEARCH EXPERIENCE

UNIVERSITY OF CALIFORNIA, SANTA BARBARA (Santa Barbara, CA)
Graduate Student Researcher, Angela Pitenis Lab & Denise Montell Lab 2019-2024

- Modeling Soft Tissue Damage by Breast Implant Associated Shear Stresses
- Collective Force Generation in Pancreatic Ductal Adenocarcinoma Organoid Models
- Cradling, Not Confining: In Vitro Mounting of Zebrafish Embryos with Microgel

JOHNS HOPKINS UNIVERSITY (Baltimore, MD)
Graduate Student Researcher, Jamie Spangler Lab 2018-2019

- Engineered antibodies exhibiting allosteric competition with endogenous Epidermal Growth Factor Receptor (EGFR) overexpression for improved therapeutic delivery.

Undergraduate Student Researcher, Wirtz Lab 2017-2018

- Characterized cancer cell migration in 2D and 3D culture to investigate density and differences in metastatic potential.

FELLOWSHIPS

Gates Millennium Scholar-Hispanic Scholarship Fund	[$500,000]	2014-2024
CNSI/MRL Alan and Ruth Heeger Fellowship	[$1,000]	2023
Connie Frank Biomedical Research Fellowship	[$9,000]	2020

HONORS/AWARDS

NIH IPERT Travel Grant ($1,800) 2023
University of California, Santa Barbara Academic Senate Travel Grant ($900) 2022
NIH IPERT Travel Grant ($1,800) 2022
University of California, Santa Barbara Academic Senate Travel Grant (declined) 2022
Most Innovated Research Poster at BMSE/MCDB 25th Annual Research Retreat 2022
1st Place, UCSB Center for Science and Engineering Program Art of Science Competition 2022
Johns Hopkins University Dean's List 2014, 2018
Boy Scout of America, Eagle Scout 2014

PEER REVIEWED PUBLICATIONS

7. Rosas, J.M., Pochitaloff, M., Bae, R., Cheng, S., Stooke-Vaughan, G., Pospisil, P., Behrens, R.L., Stromf, A., Campas, O., Pitenis, A.A. Cradling, Not Confining: In Vitro Mounting of Zebrafish Embryos with Microgel. (2024). In Review at Soft Matter.
6. Rosas, J.M., Campanale, J.P., Harwood, J.L., Bae, R., Cheng, S., Tsou, J.M., Kaiser, K.M., Engle, D.D., Montell, D.J., Pitenis, A.A. Pancreatic Ductal Adenocarcinoma Organoids Exhibit Pulse-Driven Collective Force Generation in Confinement. (2024). In Review at American Chemical Society, Applied Biomaterials.
5. Atkins, D.J, Rosas, J.M., Månsson, L.K., Shahverdi, N., Dey, S.S., Pitenis, A.A. 3D Microgel Platform to Investigate Mechanical Memory in Pancreatic Ductal Adenocarcinoma. (2024). DOI: 10.1021/acsbiomaterials.3c01079.
4. Atkins, D.J., Chau, A.L., Rosas, J.M., Chen, Y.T., Chan, S.T., Urueña, J.M., Pitenis, A.A. Silicone Implant Surface Roughness, Friction, and Wear. (2022). DOI:10.1088/2051-672X/ac9f5a
3. Rosas, J.M, Atkins, D.J, Chau, A.L, Chen, Y., Bae, R., Cavanaugh, M., Espinosa Lima, R., Bordeos, A., Bryant, M., Pitenis, A. In Vitro Models of Soft Tissue Damage by Implant-Associated Frictional Shear Stresses. Journal of Engineering Tribology: Part J. (2022). DOI: 10.1177/13506501221132897.
2. Ludwig SD*, Bernstein ZJ*, Agatemor C, Dammen-Brower K, Ruffolo J, Rosas J.M, Post JD, Cole RN, Yarema KJ, Spangler JB. A versatile design platform for glycoengineering therapeutic antibodies. MAbs. 14(1):2095704. DOI: 10.1080/19420862.2022.2095704.
1. Chau, A.L, Rosas, J.M, Degen, G. D., Månsson, L. K., Chen, J., Valois, E., and Pitenis, A.A. Aqueous Surface Gels as Low Friction Interfaces to Mitigate Implant-Associated Inflammation. Journal of Materials Chemistry B. 6782-6791. (2020). https://doi.org/10.1039/D0TB00582G.

OTHER PUBLICATIONS

1. Campanale, J.P, Rosas, J.M. Mentoring with Pride. American Society for Cell Biologists, LGBTQ+ Newsletter. (2023).

PODIUM PRESENTATIONS (presented by the first author)

3. Rosas, J.M., Campanale, J.P., Harwood, J.L., Pitenis, A.A., and Montell, D.J. Fibrosis to Fitness: Examining the Role of Tumor Stiffness in Pancreatic Ductal Adenocarcinoma. American Society of Cell Biologists CellBio (2022). Washington, D.C., USA.
2. Rosas, J.M., Atkins, D.J., Chau, A.L., Chen, Y-T., Bae, R., Cavanaugh, M.K., Espinosa Lima, R.I., Bordeos, A., Bryant, M.G., Pitenis, A.A. In Vitro Models of Soft Tissue Damage by Implant-Associated Frictional Shear Stresses. Society of Tribology and Lubrication Engineering Annual Meeting (2022). Orlando, Florida, USA.
1. Rosas, J., Pitenis, A., and Montell, D. Mechanics to Metastasis- A Novel Mode of Migration (oral presentation). University of Massachusetts, Amherst: Soft Solids and Complex Fluids Symposium (2020). Virtual

POSTER PRESENTATIONS (presented by the first author)

7 Rosas, J.M., Campanale, J.P., Harwood, J.L., Bae, R., Cheng, S., Tsou, J.M., Kaiser, K.M., Engle, D.D., Montell, D.J., Pitenis, A.A. Investigating Collective Force Generation in Epithelial Organoid Models of the Pancreatic Duct. Janelia 4D Cellular Physiology Annual Meeting. (2024). Ashburn, VA.
6. Rosas, J.M., Harwood, J.L., Campanale, J.P., Pitenis, Montell, D.J., Pitenis, A.A. Pancreatic Adenocarcinoma Organoids Overcome Confinement through Collective Force Generation. American Society for Cell Biologists. CellBio23 (2023). Boston, MA.
5. Rosas, J.M., Harwood, J.L., Campanale, J.P., Pitenis, Montell, D.J., Pitenis, A.A. Murine Pancreatic Cancer Organoid Morphology and Dynamics in 3D. Cold Spring Harbor Labs Biology of Cancer: Microenvironment & Metastasis (2023). Long Island, New York.

4. Rosas, J.M., Harwood, J.L., Bae, R., Cheng, S., Campanale, J.P., Montell, D.J., Pitenis, A.A. In Vitro Dynamics of Pancreatic Cancer Organoids in 3D . Biomedical Engineering Society Annual Meeting (2023). Seattle, Washington.
3. Rosas, J.M., Campanale, J.P., Harwood, J.L., Pitenis, A.A., and Montell, D.J. Fibrosis to Fitness: Examining the Role of Tumor Stiffness in Pancreatic Ductal Adenocarcinoma. American Society of Cell Biologists CellBio (2022). Washington, D.C., USA.
2. Rosas, J.M., Campanale, J.P., Harwood, J.L., Pitenis, A.A., and Montell, D.J. Deciphering the Role of Extracellular Matrix Mechanics in Pancreatic Ductal Adenocarcinoma. Molecular, Cellular, and Developmental Biology and Biomolecular Science and Engineering Retreat (2022). Santa Barbara, CA. USA.
1. Rosas, J.M., Campanale, J.P., Harwood, J.L., Pitenis, A.A., and Montell, D.J. Mechanosensation in Disease: Pancreas Organoids as a Model for Disease Progression. Bioengineering Research Symposium and Biotechnology Industry Showcase (2022). Santa Barbara, CA, USA.

PROPOSALS & WHITEPAPERS

2. Cancer Research Coordinating Committee, UCSB. Investigating the Molecular and Transcriptional Adaptations to 3D Confinement in Human and Murine Pancreatic Ductal Adenocarcinoma Organoid Models
1. W.M. Keck Foundation. Mu-Taxis: The role of Frictional Shear Stress in Pancreatic Ductal Adenocarcinoma

TEACHING EXPERIENCE

Teaching Assistant, University of California, Santa Barbara

Introduction to Chemical Engineering Design Fall 2019

- Undergraduate-level chemical engineering course introducing first-year students to the mathematical techniques necessary to approach core design principles in chemical engineering: mass, momentum, and energy balances, economic analysis.

OUTREACH

Panelist, Center for Science and Engineering Partnerships

- Preparing for Graduate School August 2023
- Aligning Expectations with Your Mentee June 2023

Mentor, UC Santa Barbara Materials Research Science and Engineering Center

- Cooperative International Science and Engineering Internships (CISEI) Program 2023
- Future Leaders of Advanced Materials (FLAM) Summer Program 2021

Presenter, Irvington High School, CA Synapsis Summer Camp July 2020

- Elementary School Introduction to Current Topics in BioEngineering/Biomaterials

Johns Hopkins University Resident Advisor 2016-2018
Mentoring Assistance Peer Program (MAPP) 2014-2018
Health Leads Patient Advocate at the Johns Hopkins Hospital 2017-2018

MENTORSHIP

UNIVERSITY OF CALIFORNIA, SANTA BARBARA (Santa Barbara, CA)

Luffy Li 2023-present
Julia Tsou 2023-present
Justine Lee 2024
Kevin Ogbonna 2022-2023
Rachel Bae, current: Scientist, Apeel 2021-2024
Kathi Kaiser, CISEI Summer Intern 2023
Shujun (Cecilia) Cheng, current: UCLA 2022-2023
Jacob Harwood, current: PhD Student, UCSB Molecular Biology 2022-2023
Daniela Semaan, current: OWL Biomedical Inc. 2021-2022

Ricardo Espinosa-Lima, current: PhD Student, UCSF, Stem Cell Biology	2021-2022
Samantha Chan, current: Research Scientist, Crosshair Therpaeutics	2021-2022
Jonathan Chen, current: Engineer, C-Zero	2020-2022
Ines Bilkic, current: Consultant Engineer FM Global	2019-2020
Steven Nguyen, current: PhD Student, UCSD	2019 - 2021

JOHNS HOPKINS UNIVERSITY (Baltimore, MD)

Benjamin Leach	2018-2019
Santiago Balza	2018-2019

Abstract

Organoids to Organisms: Engineering 3D Microenvironments to Support Biological Systems

by

Jonah Mathew Rosas

The microenvironment plays a central role in supporting a diverse set of cell functions ranging from cell fate decisions that specify cell lineage during early embryonic development to single-cell and organ-scale size regulation. In the past two decades, a renewed emphasis has been placed on the mechanical microenvironment and its role in healthy and disease biology.

In this dissertation, I describe the rheology of granular, polyacrylamide hydrogels composed of micron-scale fragments, herein referred to as microgels, and demonstrate their utility in supporting the extended imaging of the model organism *danio renio (zebrafish)* and for controlling the mechanical microenvironment encapsulating pancreatic ductal adenocarcinoma organoids. This work addresses two long standing challenges in the field: 1) Microgels offer an engineered embedding method that extends zebrafish embryonic imaging times by 8× compared to field standards. 2) Pancreas ductal adenocarcinoma (PDAC) organoids exhibit an emergent pulsing behavior that is enhanced in confining microgel environments, suggesting the

underlying genetics of tumor cells give rise to force generating behaviors that may be assistive for adaptation to highly fibrotic tumor microenvironments *in vivo.*

Table of Contents

Acknowledgements ..... *v*

Vita Of Jonah Mathew Rosas ..... *x*

Abstract ..... *xiv*

List of Figures *15*

CHAPTER 1: Dissertation Overview *1*

CHAPTER 2: Cradling Without Constraining: Supporting Imaging of Shape-Changing Biological Samples *2*

CHAPTER 3: Pancreatic Ductal Adenocarcinoma Organoids Exhibit Pulse-Driven Collective Force Generation in Confinement *28*

Chapter 4: Concluding Remarks and Perspectives *70*

CHAPTER 1: Dissertation Overview

Herein, I will describe the development, characterization, and implementation of a granular hydrogel technology, referred to as microgels, to study two model systems that span length scales. **Chapter 2** begins at the millimeter-scale where we optimize the rheological properties of microgels to support the extended imaging of the model organism, *danio rerio*. Through controlling the polymer concentration within individual microgel particles, we identified the material properties relevant for supporting extended embryo imaging and stable positioning. More broadly, we describe how the microenvironmental mechanics of an embedding medium is essential for supporting organismal development. **Chapter 3** zooms into the micron-scale where we develop a microgel-Matrigel^{TM} composite to support the extended culture of tissue-derived, murine, pancreas ductal organoids derived healthy and pancreatic ductal adenocarcinoma (KPC) mice. Simple microgel-Matrigel^{TM} composites created new confined microenvironments to investigate the adaptive mechanisms utilized by self-organizing, pancreas epithelia to overcome distinct mechanical microenvironments. We identified emergent, collective behaviors that are attenuated by the mechanical microenvironment in pancreatic ductal adenocarcinoma organoids and provide evidence to the molecular players regulating this behavior. **Chapter 4** concludes this thesis with perspectives and future directions for extending the utility of microgel technologies and the emergent behaviors in organoid systems.

CHAPTER 2: Cradling Without Constraining: Supporting Imaging of Shape-Changing Biological Samples

This section is adapted from a manuscript of identical title currently submitted for peer review at Soft Matter.

Jonah M. Rosas*, Marie Pochitaloff*, Petr Pospíšil, Lufei Li, Rachel Bae, Shujun Cheng, Justine Lee, Georgina Stooke-Vaughan, Rachel L. Behrens, Amanda Strom, Otger Campàs, and Angela A. Pitenis

(*equally contributed to this work)

Abstract

Significant advances in light microscopy and genetic labeling have enabled many discoveries in developmental biology. Imaging developing embryos requires properly holding the embryo in place, while not constraining its development. In inverted microscopes, the most widely used mode of microscopy, embryos are generally held in place by embedding them in gels that physically constrain them, precluding long-term imaging as the embryo changes morphology. In this study, we show that granular polyacrylamide hydrogels (microgels) mechanically support embryos in 3D while simultaneously enabling normal and unconstrained embryonic morphogenesis over time, enabling imaging of embryonic development over long times scales in inverted microscopes. We characterized the mechanical and optical properties of microgels and identified a range of microgel yield stresses that enables long-term imaging of developing zebrafish embryos.

1.0 Introduction

Since Robert Hooke's first observations of cells with his newly-invented optical microscope in the mid-1600's, discoveries in biological systems have often accompanied technological advancements in optical microscopy[1]. For over four decades, light microscopy has enabled breakthroughs in the fields of cell and developmental biology, genetics, regeneration, immunology, and oncology[2–4]. Imaging of cells in culture or other in vitro 2D systems popularized the use of inverted microscope configurations, which have become the most widely adopted configuration in light imaging. However, imaging of 3D systems, such as organoids or developing embryos, imposes specific constraints. During embryonic development or organoid growth, 3D tissues change their shapes, sometimes dramatically. Common techniques to mount embryos for imaging in inverted microscopes make use of hydrogels (e.g., agarose) to immobilize the sample in 3D. This process also physically constrains the sample, preventing its normal development after a relatively short time. Recent studies have aimed to maintain embryo positioning with patterned molds or by embedding embryos in agarose and removing the agarose around the regions that substantially change shape, [5,6] but no embedding media has yet been designed to support continuous imaging of embryonic development in inverted microscopes.

Granular hydrogel ("microgel") media present a possible embedding strategy to support long-term, continuous imaging of embryos. Microgels are particles of crosslinked hydrogel (>95% water) with tunable sizes, ranging from a few micrometers to millimeters. Microgel particles settle to form granular beds capable of supporting living systems, from single cells to tissues [7–9], which also enables media perfusion due

to their granular nature[10–13]. Unlike embedding media like bulk hydrogels, such as agarose or polyethylene glycol, that display large yield stress once crosslinked and mechanically constrain the samples, microgels locally yield in response to low stress and rapidly re-solidify at rest.[14] Moreover, it is possible to tune the yield stress by changing the material properties of the microgel particles,[7,15] providing a way to tailor microgels to suit the needs of different organisms and their growth conditions. If the yield stress of the microgel is such that it can hold the weight of the embryo but remains below the mechanical stresses associated with embryonic development, then it should be possible to hold the sample in place while imaging its development in 3D, even if it involved substantial morphogenetic changes. Their low yield stress, the possibility to tune yield, and the ability to perfuse media, make microgels an ideal candidate as imaging support media (mounting media) for shape-changing biological samples, from embryos to organoids.

In this study, we developed microgel formulations and characterized their rheological and optical properties. We demonstrate that several formulations are well-suited for imaging the development of zebrafish embryos over long time periods that involved dramatic shape changes, from early stages of development through tail eversion. Our results indicate that microgel formulations with yield stress between $0.3 < \sigma_y < 3$ Pa are optimal for maintaining embryo positioning while allowing tail eversion, whereas microgel yield stresses $\sigma_y > 3$ Pa constrained embryos and inhibited normal embryogenesis. Our study demonstrates the first instance of whole embryo imaging within microgel media capable of cradling without constraining growth.

2.0 Materials and Methods

2.1 Hydrogel Synthesis

Acrylamide (AAm), N,N′-methylene- bis(acrylamide) (MBAm), N,N,N′,N′-tetramethylethylenediamine (TEMED), and ammonium persulfate (APS) were purchased from Sigma-Aldrich® and used as received. Stock solutions of AAm (30 wt.%), MBAm (2 wt.%), TEMED (10 vol.%, corresponding to 7.9 wt.%), and APS (10 wt.%) were prepared in ultrapure deionized (DI) water (18.2 MΩ·cm). Polyacrylamide hydrogels were synthesized at polymer contents ranging from 2.3–3 wt.% AAm with a crosslinker concentration of 0.12 wt.% MBAm.

2.2 Microgel Processing

Bulk hydrogels were mechanically processed and sorted by Stokes' sedimentation to achieve a uniform distribution of particles as described in Atkins et al.7 Successive rounds of sedimentation reduced particle size heterogeneity and achieved a final sample with average particle diameter ≈100 μm. Microgels were imaged using a Nikon Ti2 Widefield Microscope with a Nikon® Ti2 Plan Widefield Microscope with a Fluor 4× (NA = 0.13) air objective. Average microgel diameters were measured by defining three points at the edge of each microgel particle and fitting a circle that contained all three points.[16] Sorted microgels were measured using the 3-point circle fitting tool in the NIS Element software to achieve final particle diameters $99.5\ \mu m \pm 16.4\ \mu m$ S.D. (n = 100 particles) (Supplementary Figure 1).

2.3 Fluorescent Nanoparticle-Embedded Microgels (Labeled Microgels)

Polystyrene green, fluorescent beads (diameter = 100 nm) were purchased from Thermo Scientific™ (Cat No. G0100) at a stock concentration of 1% solids with excitation and emission spectra (Ex. 468 nm/Em. 508 nm). Fluorescent nanoparticles were sonicated for 5 min to reduce aggregation prior to mixing into the pre-polymerized hydrogel solution. Nanoparticle-embedded microgels were synthesized with 0.01 wt.% green, fluorescent nanoparticles (diameter = 100 nm) in the pre-polymerized hydrogel solution.

2.4 Microgel Rheology

Unlabeled microgel particles were equilibrated in ultrapure water for 24 h prior to rheology measurements. Immediately before testing, microgels were centrifuged at 1,000×G for 10 min to fully jam the microgel particles, and all supernatant above the gel layer was aspirated. Jammed microgel rheology was measured using a TA Instruments ARES G2 strain-controlled rotational rheometer fitted with 50 mm diameter, stainless steel, parallel plate (401968.901) upper and lower geometries. Upper and lower plates were cleaned with ethanol prior to testing and between samples. Measurements were conducted at ambient conditions 23 ºC with a constant gap height of 500 µm, spanning approximately five microgel particle diameters.

Average storage moduli (G´) were determined in the linear viscoelastic region for each sample during amplitude sweeps conducted at a frequency, f = 1 rad/s. Average yield stresses, σ_y, were calculated at the crossover point where the storage and loss moduli intersect (G´ = G´´), determined using a linear and cubic spline combination

(Cubic/Linear (Orche) method in the Trios software) well described in other studies of microgel rheology.[17,18]

2.5 Microgel UV-Vis Spectrophotometry

Microgels were equilibrated for 48 h in either ultrapure water, 1× PBS, or 4X PBS prior to experimentation. Microgels were transferred to a polystyrene disposable cuvette with a 1 cm (Fisher Scientific:14-955-129) or custom 500 µm path length and overlaid with additional solvent (ultrapure water, 1× PBS, or 4× PBS). UV-VIS measurements were conducted using a Shimadzu™ UV3600 UV-Nir-NIR spectrometer over wavelengths 350 – 850 nm with a 3 nm slit width and 5 nm step in wavelength with an absorbance stage configuration. All measurements were conducted relative to a media blank set in the reference position at the time of testing. Absorbance data were transformed to transmittance (%) following Equation 1:

$$transmittance\ (\%) = 10^{2-absorbance} \qquad (1)$$

2.6 Microgel Point Spread Function Characterization

The Point Spread Function (PSF) was determined for 2.5, 2.55, and 3 wt.% microgels and 0.5 wt.% agarose embedded with 100 nm green fluorescence beads at 0.01 wt.% (TetraSpeck™, Invitrogen and Thermo Scientific (G0100)). Microgels and agarose were deposited in a 96 glass-bottomed well plate (Greiner Bio-One®) and were imaged using a laser scanning confocal microscope (LSM 980 with Airyscan 2, Carl Zeiss) running the software ZEN Blue (Carl ZEISS) at room temperature. Stacks of voxel size 28×28×100 nm were acquired for each sample using a 40× water immersion objective

(LD C-Apochromat 40╳/1.1W, Carl ZEISS Inc.) with 488 nm excitation and 488–588 nm detection in confocal mode with 1 AU pinhole size.

Data were analyzed using a custom-made Python code implemented in Jupyter™ notebook and adapted from the GitHub notebook managed by B. Nitzsche and R. Haase. For 0.5% agarose (n = 28), 2.50 wt.% microgel (n = 30), 2.55 wt.% microgel (n = 22), and 3 wt.% microgel (n = 35), 100 nm nanoparticles embedded within the samples were analyzed separately and averaged to obtain the mean Full Width at Half Maxima (FWHM).[19] Individual particle intensities were averaged to obtain an averaged PSF and averaged FWHM for each sample.

2.7 Zebrafish husbandry, lines and experimental manipulations.

Zebrafish (Danio rerio) were maintained under standard conditions20. Animal husbandry and experiments were conducted according to all ethical regulations and protocols approved by the Institutional Animal Care and Use Committee (IACUC) at the University of California Santa Barbara (protocol number 886) and by the European Union (EU) directive 2010/63/EU as well as the German Animal Welfare act. Tg(actb2:mem-NeonGreen)hm37 and Tg(actb2:MA-mCherry2)hm2 transgenic lines were used for ubiquitous labeling of cell membrane of zebrafish embryos and Tg(h2afva-GFP) × Tg(actb2:MA-mCherry2)hm29 double transgenic line was used to visualize nuclei and membrane of zebrafish embryos.

2.8 Zebrafish Mounting

Prior to the sample mounting, microgels were centrifuged to yield a jammed gel layer. 150 µL of microgel was added to each well of a 96-well glass-bottomed 96-well

plate (CellVis 96-Well Glass-Bottomed Plate (#0 Glass, 6mm well size)). A dechorionated zebrafish embryo was gently added to each well and manually placed within 1 mm of the cover glass. E2 buffer with 0.2 g/L tricaine methanesulfonate (MS-222) of pharmaceutical grade (Western Chemical) was added to each well.

2.9 Zebrafish Imaging

Images were acquired using both a Zeiss LSM710 and LSM 980 laser scanning confocal microscopes with 10× air, 10× water, or 40× water objective at 25 ° C. Time-course imaging was captured at 15- or 30-min intervals. Tail elongation was recorded by 3D tiling using the Airyscan mode of the LSM 980 confocal. Images were processed using ZEN Blue (Carl ZEISS) to generate maximum intensity projections.

3.0 Results and Discussion

3.1 Microgels exhibit tunable rheological properties

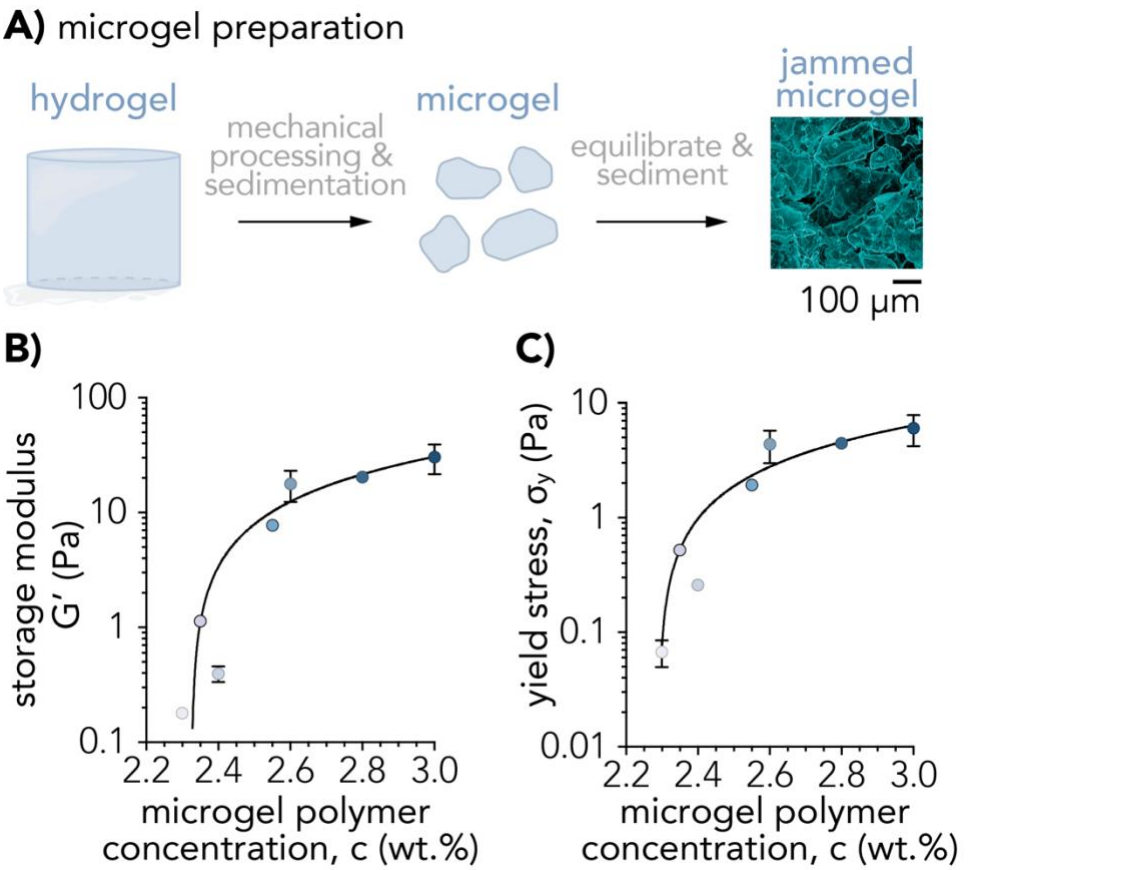
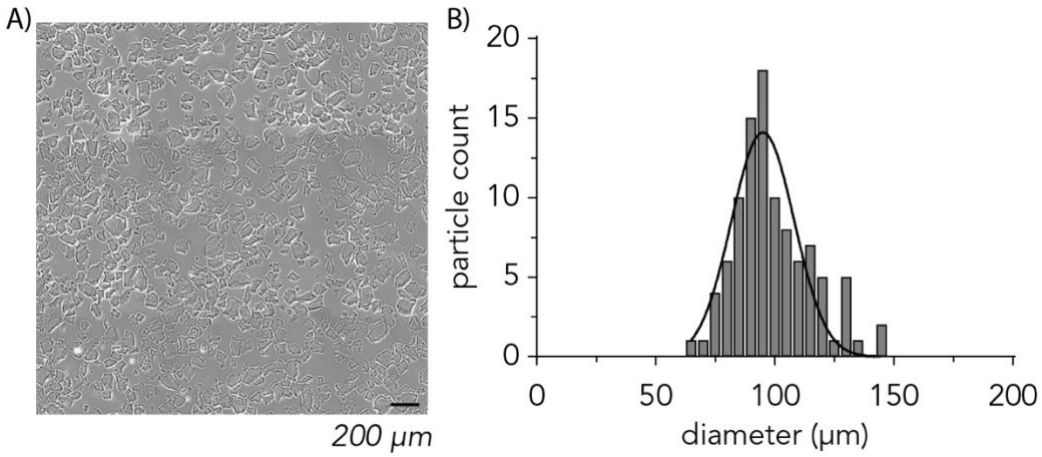


Figure 1. Mechanical tunability over a range of microgel particle polymer contents. A) Schematic of microgel processing from bulk polyacrylamide hydrogel to microgel particles with diameter of approximately 100 µm. Jammed microgel boundaries visualized in cyan using 100 nm green beads to decorate the gel surface. Microgels were characterized with a parallel plate rheometer (50 mm diameter plates). **B**) Microgel storage modulus (n = 2) and **C**) yield stress (n=2) as a function of microgel polymer content (wt.%). First-order polynomial fits serve as guide lines.

The rheological properties of jammed microgels (Figure 1A) were characterized using a strain-controlled rheometer with a parallel plate geometry at ambient temperature. Microgel storage modulus, G´, was evaluated at the plateau region over low strains (Figure 1B). Storage modulus, G', generally increased with polymer concentration of the microgels, c, from G´ = 0.18 ± 0.02 Pa to G´ = 30.64 ± 8.94 Pa for c = 2.3 wt.% to c = 3 wt.% microgel polymer concentration, respectively. The storage modulus versus microgel polymer concentration data is overlaid with a first-order polynomial fit as a guideline.

Our results deviate strongly from the conventional scaling relationship put forth by de Gennes (G´~ 3c9/4) for semi-dilute concentrations[15]. The power-law fit worsens as microgel polymer concentration decreases from c = 3.0 wt.% polymer. Although the microgels in this study are composed of covalently-crosslinked hydrogels, the polymer concentration within individual microgel particles may be so low that they may be on the cusp of the semi-dilute regime. Microgel yield stress (σ_y) was evaluated at the crossover point of the storage modulus, G´, and loss modulus, G´´, the point at which microgel particles become unjammed and flow is induced in the system. Yield stress increased from σy = 0.07 ± 0.02 Pa to σy = 6.05 ±1.82 Pa for c = 2.3 wt.% to c =3 wt.% microgel polymer concentration, respectively (Figure 1C).



Supplementary Figure 1: Microgel Particle Diameter Measurements A) Representative brightfield imaging of sorted microgel particles with a **B**) size distribution of 99.5 μm ± 16.4 μm.

The yield stress versus microgel concentration data is fit with a first-order polynomial fit as a guideline. Yield stress scaled with storage modulus following a power law relationship (Equation 2).

$$\sigma_y = 0.5 \times G'^{\frac{3}{4}} \qquad (2)$$

These results show that microgels exhibit tunable rheological properties where storage modulus and yield stress follow a scaling relationship (σy ~ G´3/4). The observed scaling relationship departs from prior studies of jammed, spherical, charged polyelectrolyte microgels (σy ~ G´1)[14] and glassy colloidal suspensions (σy ~ G´2.13).[21] Such differences may be attributed to the non-spherical and irregular geometries of the polyacrylamide microgels used in this study, underscoring the importance of microscale particle geometry on macroscale rheology of jammed microgel systems. This highlights the importance of both polymer chemistry and particle geometry on governing the macroscale rheology of jammed microgel systems.

3.2 Microgels scatter incident light as a function of path length

A central component of any 3D culture medium is optical compatibility with optical microscopy setups and high-resolution imaging. To match the working distances of high-resolution objectives, we determined the transmittance of microgels containing 2.3, 2.4, 2.5, 2.6, 2.7, 2.8, and 3.0 wt.% polymer concentration by UV-Vis spectrophotometry over a 500 µm path length (Figure 2A). The UV-Vis results suggest that all microgel compositions transmitted at least 80% of incident light across 500 µm path lengths (Figure 2B), with higher transmittance for lower concentrations and wavelength-independent transmittance in the visible range in all cases.

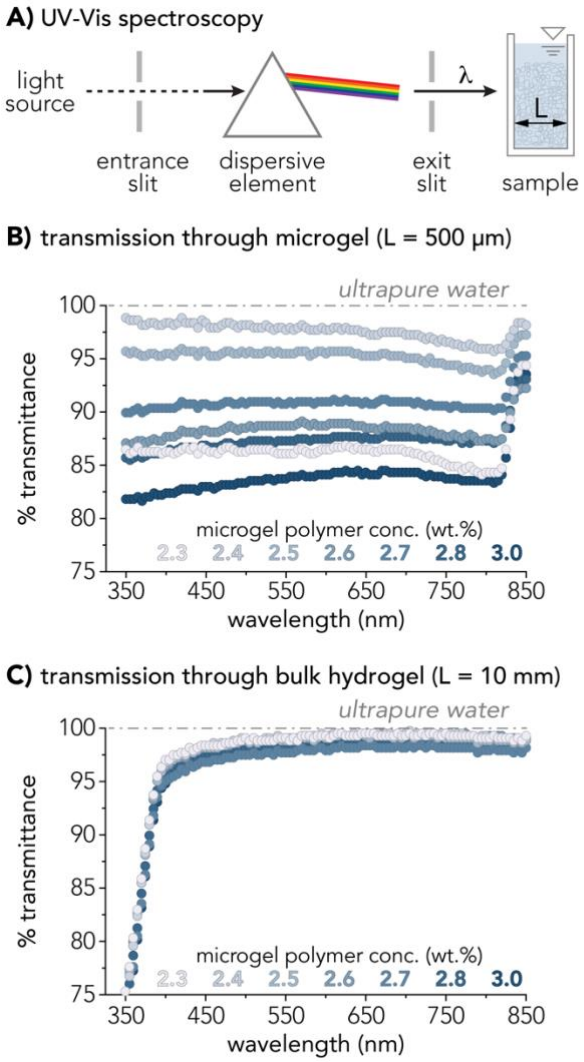
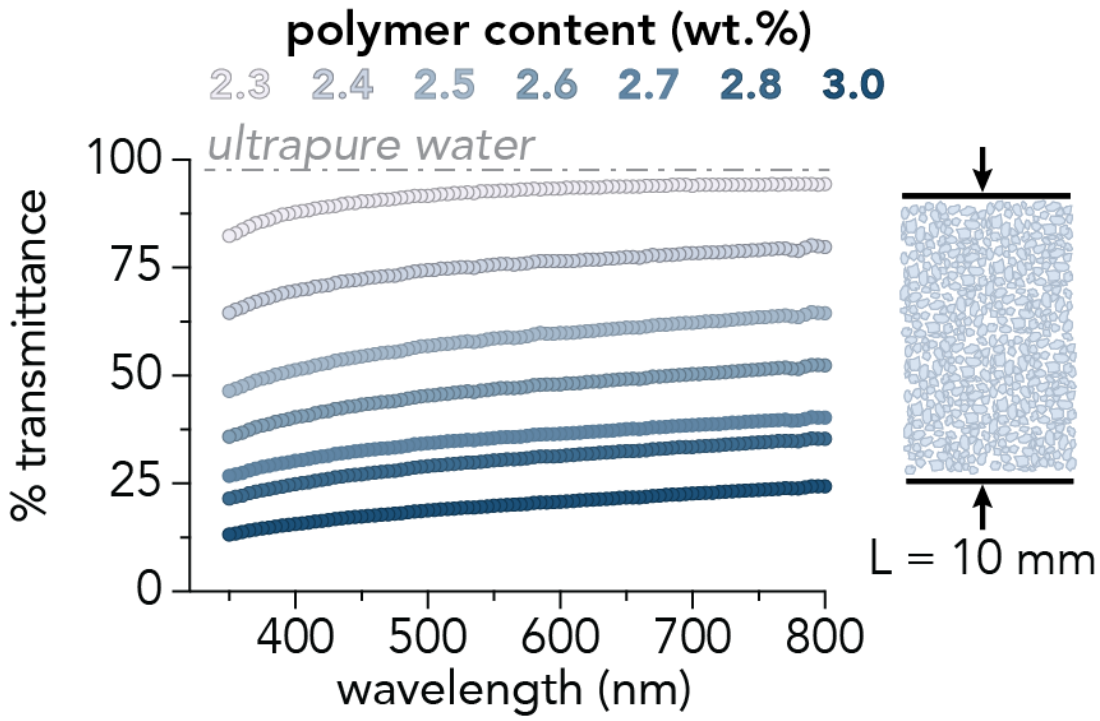


Figure 2. Microgel particles scatter light at gel edges. A) Schematic of UV-Vis spectrophotometry characterization of microgels. **B**) Microgel UV-Vis transmittance spectra over a 0.5 mm pathlength. **C**) Bulk hydrogel UV-Vis transmittance spectra over a 10 mm pathlength.

Over longer path lengths (L = 10 mm, Supplementary Figure 2), transmittance in microgels decreased as a function of microgel polymer content: 2.3 wt.% microgels achieved over 75% transmittance while 3.0 wt.% microgels achieved less than 25% transmittance.

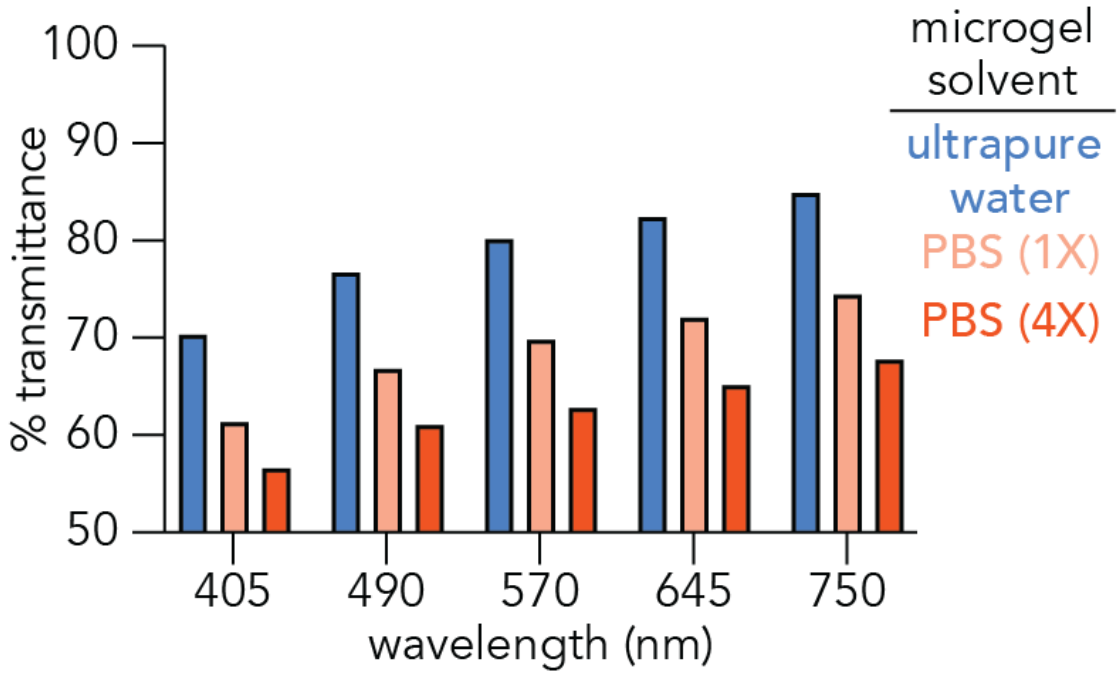


Supplementary Figure 2: 10 mm Pathlength UV-Vis Measurements

These findings are consistent with the Beer-Lambert Law that dictates transmittance of incident light is related to the length of the beam path and concentration of the absorbing species through which the beam travels.[22]

Microgel measurements at both long and short path lengths supported the hypothesis that decreases in transmittance were due to a combination of scattering at the edges of microgel particles and absorbance of light by polyacrylamide itself. To address the latter, we determined the transmittance of bulk polyacrylamide hydrogel samples cast at identical polymer content as tested microgels (Figure 2C). UV-Vis measurements of bulk hydrogel samples maintained >90% transmittance across the visible light spectrum with absorbance seen only at wavelengths below 350 nm where prior studies have found polyacrylamide to begin absorbing energy.[23] Taken together,

these data demonstrate polyacrylamide hydrogels do not absorb light across the UV-visible spectrum relevant for optical imaging but rather scatter light when processed into microgels. These results agree with the Beer-Lambert Law described for absorbing species and expand the applicability of the principle to species that significantly scatter light rather than absorb. Solvent salinity also reduced microgel transmittance. When swollen in 4✕ PBS, 2.55 wt.% microgel transmittance was reduced by approximately 15% in the 405, 490, 570, 645, and 750 nm wavelengths (Supplementary Figure 4).



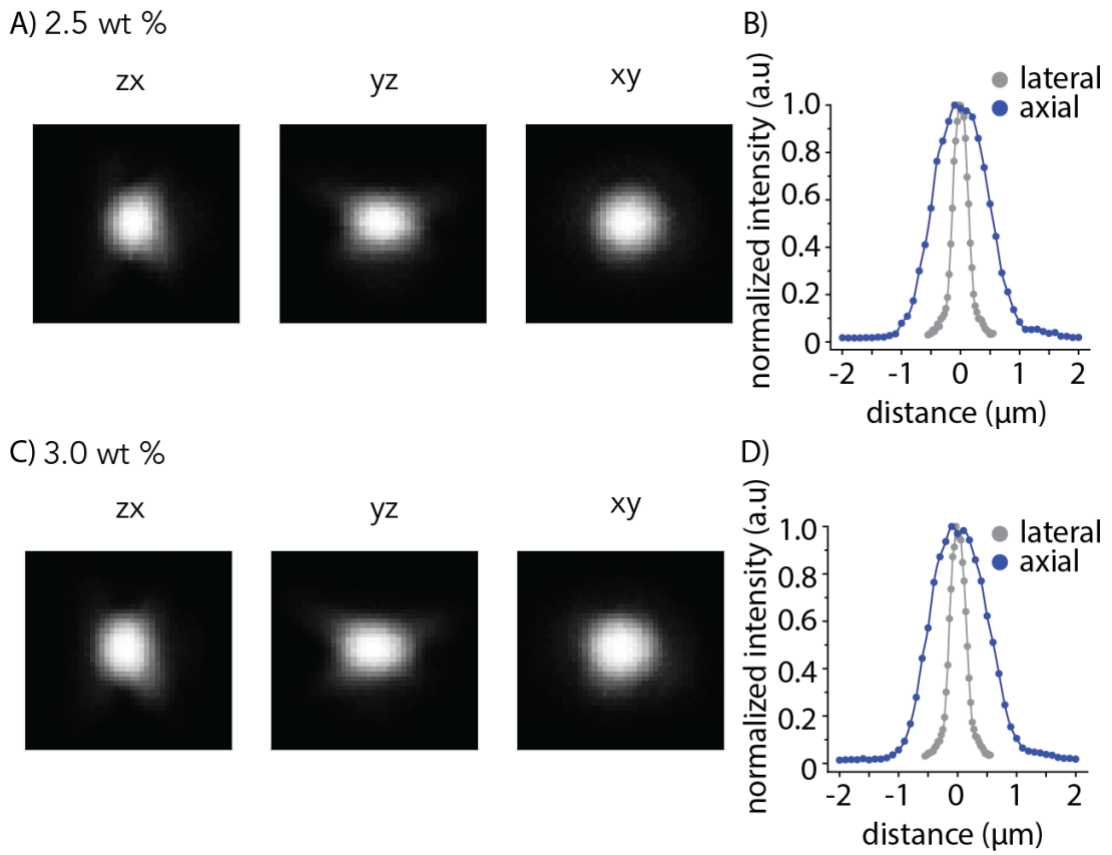
Supplementary Figure3: 10 mm Pathlength UV-Vis Measurements of 2.55 wt.% microgel swollen in ultrapure water, 1✕ PBS, or 4✕ PBS.

Our findings indicate microgels are optically compatible with fluorescent microscopy applications with considerations given both to the pathlength for imaging and the solvent used for swelling the microgels.

3.3 Microgels maintain confocal resolution with minimal distortions of fluorescent point sources

An effective 3D embedding medium compatible with high resolution optical imaging, and especially confocal imaging, should not significantly distort fluorescent signal. A classical approach to determining how a material alters a fluorescence point source is the determination of the Point Spread Function (PSF), an operation where a sub-diffraction sized, fluorescent bead is imaged and reconstructed in the axial (xy) and lateral (yz) dimensions. The imaging resolution is reduced as the PSF of a material widens compared to the theoretical Airy disk.[19]

To describe changes in imaging resolution by microgels, we determined the PSFs of 2.5, 2.55 and 3.0 wt.% microgels, as well as 0.5 wt.% agarose as a reference media for optical imaging (Figure 3, Table 1, Supplementary Figure 4). We embedded green polystyrene nanoparticles (d = 100 nm) in each sample and obtained the average PSFs (Figure 3A,C and Supplementary Figure 4A, C), which were generated by computationally superimposing all measured PSFs for a given condition 24. We then obtained the average full-width at half-maximum (FWHM) of the PSF along the lateral (xy) and axial (yz) dimensions in each condition (Figure 3B, D and Supplementary Figure 4B, D).



Supplementary Figure 4: Point–Spread–Function and Full Width at Half Maximum Measurements of 2.5 and 3 wt.% Microgels A) 2.5 wt.% microgel superimposed PSF and **B**) intensity profiles in the lateral and axial dimensions. **C**) 3.0 wt.% microgel superimposed PSF and **D**) intensity profiles in the lateral and axial dimensions.

All units: nanometers	FWHM	0.5 wt.% agarose n = 29	2.5 wt.% microgel n = 31	2.55wt.% microgel n = 22	3wt.% microgel n = 35
Individual PSF	Lateral	292 ± 29	306 ± 36	321 ± 30	322 ± 29
	Axial	782 ± 96	859 ± 124	922 ± 136	921 ± 131
Superimposed PSF	Lateral	305	299	314	319
	Axial	805	869	909	929

Table 1: Full–Width–Half–Max Measurements for agarose (green) and 2.5, 2.55 and 3 wt.% microgels (blue).

The PSFs of reference 0.5 wt.% agarose gels had an averaged FWHM in the lateral direction of d_{xy} = 292 ± 29 nm and in the axial direction of d_{yz} = 782 ± 96 nm (Figure 3F, G). We found that the FWHM of microgels of different concentrations was slightly

larger (~10%) than that of the reference agarose gel (Figure 3F,G). Our highest polymer content microgels require a minimum of 150 nm spacing to resolve fluorescent objects in the axial direction and 30 nm to resolve in the lateral direction. These findings demonstrate that microgels have the appropriate light transmission properties for highly resolved imaging and achieve comparable resolution to standard agarose mounting media.

3.4 Microgels support long-term imaging of zebrafish embryos with inverted microscope configurations

Over the past decade, a growing body of research use microgels to support sample embedding, from 3D cell printing to controlled-release drug delivery, [7,9,32,12,25–31] as they provide mechanical support and allow media perfusion. However, microgels have not yet been adapted to study embryonic development of model organisms undergoing substantial shape changes.

To use microgels as imaging media for studying embryonic development, it is necessary to find the range of microgel concentrations that can physically support the embryo in 3D, and simultaneously allow it to develop normally (Figure 4A). Microgels with yield stresses below 0.1 Pa failed to hold the embryo at a given spatial position, with the embryo tilting and sinking over the first few minutes of imaging (Figure 4B,D). Microgels with yield stresses between $0.3 < \sigma y < 3$ Pa were optimal for maintaining embryo positioning in 3D while simultaneously allowing normal development (Figure 4B). Microgels with yield stresses $\sigma y > 3$ Pa confined developing embryos and physically restricted 3D shape changes, preventing normal tail extension (Figure 4B, C).

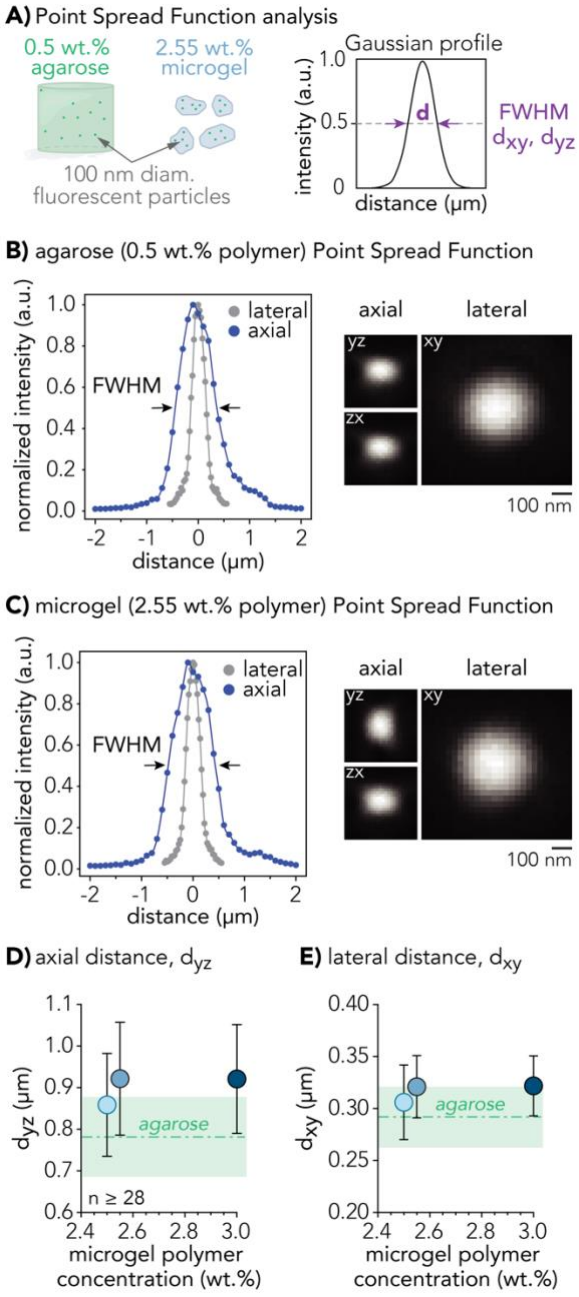


Figure 3. Point Spread Function of fluorescent particles in microgels versus agarose. **A**) Schematic of the PSF intensity profile with the Full Width at Half Max (FWHM) given by distance, d. **B**) Intensity profiles and superimposed PSFs of 0.5 wt.% agarose in the axial (blue) and lateral dimensions (grey). **C**) Intensity profiles and superimposed PSFs of 2.55 wt.% microgel in the axial (blue) and lateral (grey) dimensions. Average FWHM measurements of 2.50, 2.55 and 3 wt.% microgels and 0.5 wt.% agarose in the **D**) axial and **E**) lateral dimensions. Fluorscent nanoparticle embedding and optimization conducted by J.M.R. PSF Data measurement and analysis conducted by M.P and P.P.

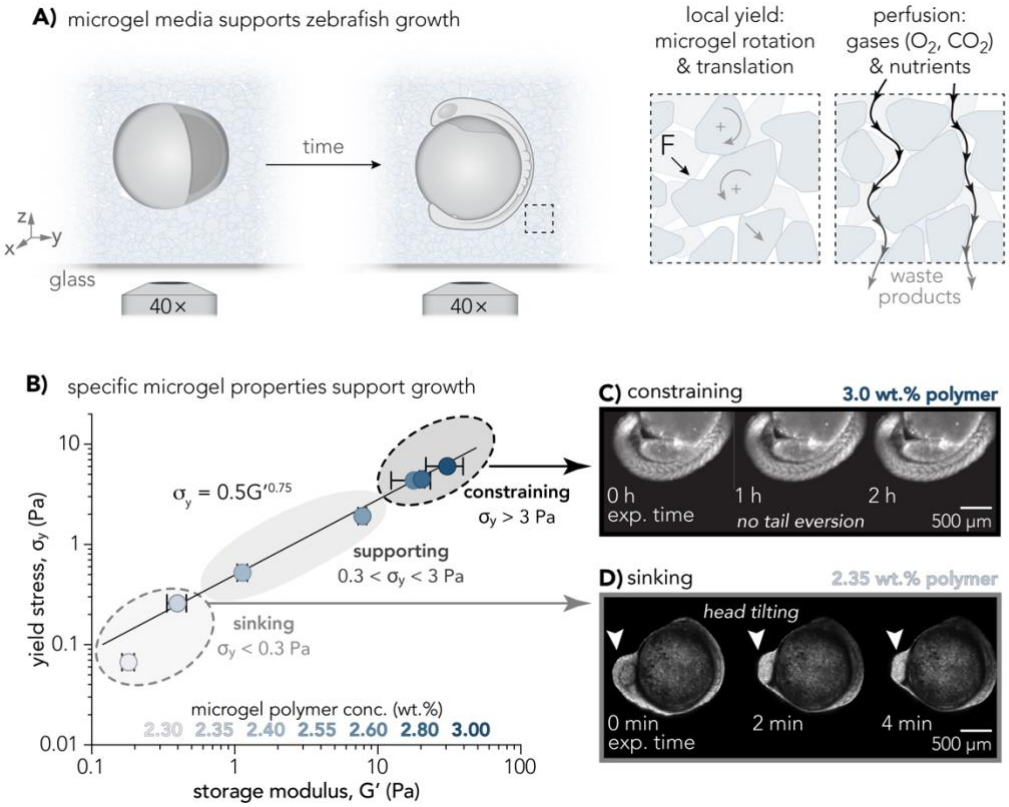


Figure 4. Optimizing microgel yield stress for zebrafish embryo embedding. **A**) Illustration of zebrafish embryo (1 mm diameter) supported in 3D by microgel media (100 µm diameter particles). First inset shows forces generated by zebrafish during development locally yield. Second inset shows microgels channels between microgel particles permit perfusion of gases and nutrients. **B**) Microgel yield stress (σ_y) plotted versus storage modulus (G') for seven different microgel polymer concentrations from 2.30 to 3.00 wt.% polymer. The solid line is the function $\sigma_y = 0.5G'^{0.75}$. Our results suggest the optimal yield stress for embedding embryos is between $0.3 < \sigma_y < 3$ Pa. Transgenic membrane labeled zebrafish embryos embedded in **C**) 3.0 wt.% microgel polymer concentration are constrained by the higher yield stress ($\sigma_y >$ 3 Pa) and are unable to undergo proper tail eversion. In contrast, embryos embedded in **D**) 2.35 wt.% microgel polymer concentration are not supported by the very low yield stress ($\sigma_y < 0.3$ Pa) and begin sinking and rotating within minutes.

Knowing the range of microgel concentrations that allow the embryo to be held in 3D while allowing normal embryonic development, we performed long-term imaging of both early stages of zebrafish embryonic development (from the 2-cell stage until the 9-somite stage; 15h period) and later stages, where dramatic shape changes occur as the zebrafish straightens its tail, a process known as tail eversion (Figure 5).

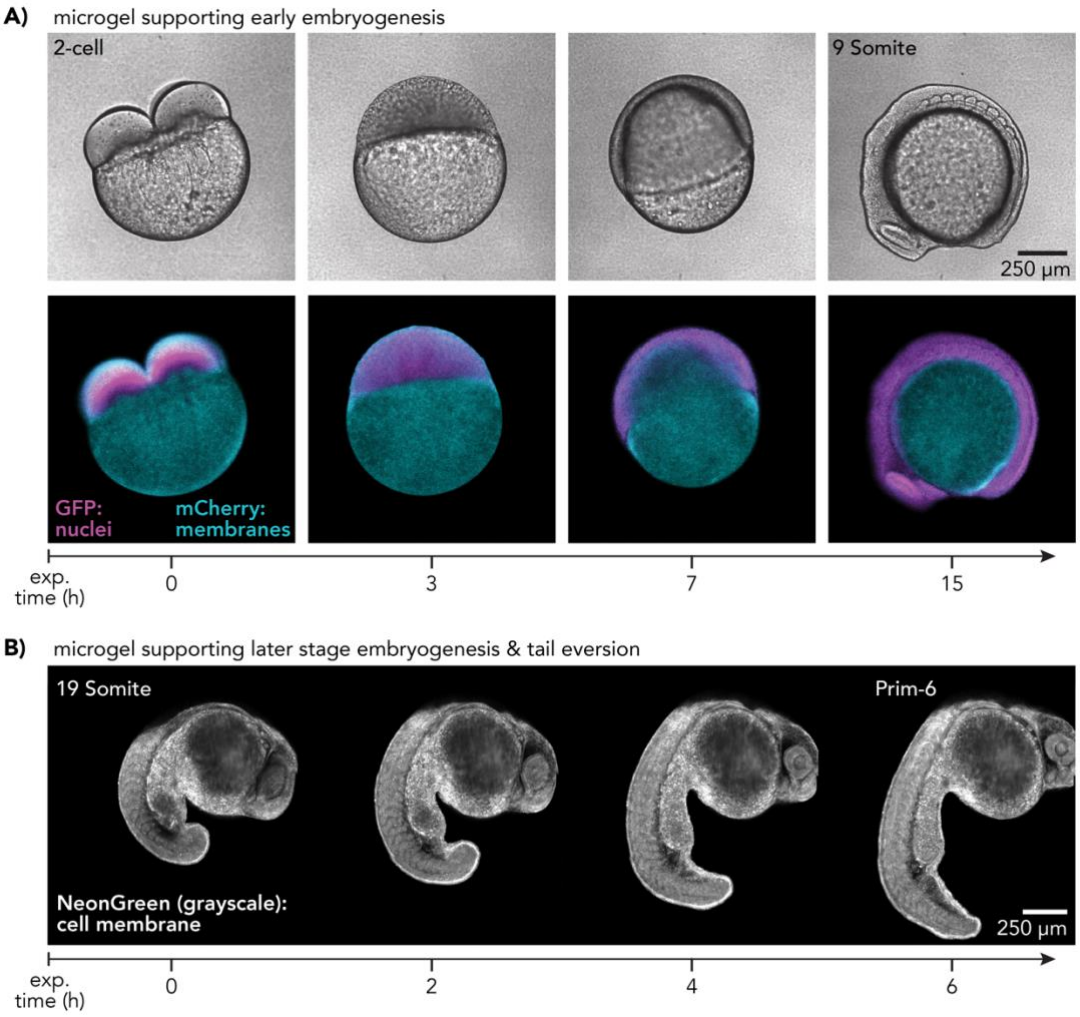


Figure 5. Microgels Support Zebrafish Embryogenesis A) Zebrafish embryo imaging from the 2-cell stage to the 9-somite stage and both T-PMT and confocal images were generated where mCherry labels cell membrane (cyan) and GFP labels cell nuclei (purple). **B**) Airyscan imaging of early tail eversion starting at the 9-somite stage to the prim-6 stage where NeonGreen labels cell membranes (grayscale). Imaging optimization was conducted by M.P. and J.M.R. while final images displayed were captured by M.P.

Imaging from the two-cell to 9-somite stages requires an embedding medium that can locally yield to accommodate embryonic shape changes. Tg(h2afva-GFP) × Tg(actb2:MA-mCherry2)hm29 double transgenic zebrafish embryos (to label nuclei and

cell membranes) were embedded in 2.45 wt.% microgels at the 2-cell stage and imaged successfully for 15 h in both transmitted light and fluorescence modes in an inverted confocal microscope (Figure 5A). We imaged embryos embedded in 2.50 wt.% microgels from the 19-somite stage (19 h post fertilization) to the prim-6 stage (25 h post fertilization), as the embryo undergoes dramatic shape changes during tail eversion at these stages. Zebrafish successfully underwent tail eversion when embedded in 2.50 wt.% microgels (Figure 5B) while being simultaneously held in place during imaging. Our findings show that microgels can be successfully used as mounting media for imaging of developing embryos: they hold the embryo in place while allowing it to develop normally, even when the embryos undergo remarkable shape changes in 3D. More broadly, microgels constitute a material system that can be used to address biological questions spanning length-scales, from single cells to whole organism.

6. Conclusions

In this study, we demonstrated that microgels can be used as mounting media to image embryonic development over long time-scales in inverted microscopes, opening new opportunities to study cellular and developmental processes in intact embryos. We described the rheological and optical properties of granular, polyacrylamide microgels, which allowed us to identify the non-linear scaling relationship between microgel storage modulus and yield stress and to obtain the path length-dependence of microgel optical clarity. We also obtained the range of microgel

concentrations for which it is possible to hold embryos in position in 3D while simultaneously enabling their proper development, even when this involved dramatic shape changes. No existing mounting media has been able to successfully support zebrafish embryonic development over such long timescales while maintaining embryo positioning. While the specific range of microgel concentrations allowing long-term imaging may depend on the organism, our results show that microgels enable long term 3D imaging of embryonic development with subcellular resolution in widely-used inverted light microscopes.

1. Microgels are rheologically tunable with yield stress scaling with storage modulus following a power-law scaling relationship.
2. Microgels maintained >80% transmittance at 500 μm pathlengths, like the working distance of most inverted microscopes.
3. Microgels minimally distort fluorescent signals – 150 nm wider in the axial and 30 nm wider in the lateral dimension compared to agarose.
4. Microgel formulations with yield stresses between 0.1–3 Pa supported zebrafish embryo imaging from the 2-cell (0.75 hpf) through the 6-prim (25 hpf) stage.

References

1. Crouvisier-Urion, K. et al. Four hundred years of cork imaging: New advances in the characterization of the cork structure. Sci. Rep. 9, 19682 (2019).

2. Link, B. A. & Megason, S. G. Zebrafish as a Model for Development. in Sourcebook of Models for Biomedical Research 103–112 (Humana Press). doi:10.1007/978-1-59745-285-4_13.

3. Serwane, F. et al. In vivo quantification of spatially varying mechanical properties in developing tissues. Nat. Methods 14, 181–186 (2017).

4. Veldman, M. B. & Lin, S. Zebrafish as a Developmental Model Organism for Pediatric Research. Pediatr. Res. 64, 470–476 (2008).

5. Schröter, C. et al. Dynamics of zebrafish somitogenesis. Dev. Dyn. 237, 545–553 (2008).

6. Hirsinger, E. & Steventon, B. A Versatile Mounting Method for Long Term Imaging of Zebrafish Development. J. Vis. Exp. (2017) doi:10.3791/55210.

7. Atkins, D. J. et al. Survival-Associated Cellular Response Maintained in Pancreatic Ductal Adenocarcinoma (PDAC) Switched Between Soft and Stiff 3D Microgel Culture. ACS Biomater. Sci. Eng. 10, 2177–2187 (2024).

8. Bhattacharjee, T. et al. Liquid-like Solids Support Cells in 3D. ACS Biomater. Sci. Eng. 2, 1787–1795 (2016).

9. Bhattacharjee, T. & Angelini, T. E. 3D T cell motility in jammed microgels. J. Phys. D. Appl. Phys. 52, (2019).

10. Sawyer, W. G. et al. Perfusion enabled bioreactor. 66 (2023).

11. Nguyen, D. T. et al. Bioconjugated liquid-like solid enhances characterization of solid tumor - chimeric antigen receptor T cell interactions. Acta Biomater. 172, 466–479 (2023).

12. Nguyen, D. T. et al. Bioconjugation of COL1 protein on liquid-like solid surfaces to study tumor invasion dynamics. Biointerphases 18, (2023).

13. Nguyen, D. T. et al. 3D In Vitro Platform for Cell and Explant Culture in Liquid-like Solids. Cells 11, 967 (2022).

14. Bhattacharjee, T. et al. Polyelectrolyte scaling laws for microgel yielding near jamming. Soft Matter 14, 1559–1570 (2018).

15. De Gennes, P.-G. Scaling concepts in polymer physics. Cornell Univ. Press (1979).

16. Garcia-Lopez, J. & Ramos, P. A. Fitting a Set of Points by a Circle. Proc. Thirteen. Annu. Symp. Cumputational Geom. (1997).

17. Ghosh, A. et al. Linear and nonlinear rheology and structural relaxation in dense glassy and jammed soft repulsive pNIPAM microgel suspensions. Soft Matter 15, 1038–1052 (2019).

18. Zhang, R. & Schweizer, K. S. Theory of nonlinear elasticity, stress-induced relaxation, and dynamic yielding in dense fluids of hard nonspherical colloids. J. Chem. Phys. 136, (2012).

19. Cole, R. W., Jinadasa, T. & Brown, C. M. Measuring and interpreting point spread functions to determine confocal microscope resolution and ensure quality control. Nat. Protoc. 6, 1929–1941 (2011).

20. Nûsslein-Volhard, C. & Dahm, R. Zebrafish: A Practical Approach. (Oxford University Press, 2002).

21. Kobelev, V. & Schweizer, K. S. Strain softening, yielding, and shear thinning in glassy colloidal suspensions. Phys. Rev. E 71, 021401 (2005).

22. Swinehart, D. F. The Beer-Lambert Law. J. Chem. Educ. 39, 333 (1962).

23. Nan, X., Sun, L., Wu, M. & Chen, G. Dark polymerization of acrylamide induced by tyrosine-containing peptide. Polym. Bull. 78, 4649–4664 (2021).

24. Nitzsche, B. & Haase, R. Determining the point-spread-function from a bead image by averaging. https://haesleinhuepf.github.io/BioImageAnalysisNotebooks/18a_deconvolution/extract_psf.html.

25. Bhattacharjee, T. et al. Liquid-like Solids Support Cells in 3D. ACS Biomater. Sci. Eng. 2, 1787–1795 (2016).

26. O'Bryan, C. S. et al. Three-dimensional printing with sacrificial materials for soft matter manufacturing. MRS Bull. 42, 571–577 (2017).

27. Bhattacharjee, T. et al. Writing in the granular gel medium. Sci. Adv. 1, 4–10 (2015).

28. Jeon, O. et al. Individual cell-only bioink and photocurable supporting medium for 3D printing and generation of engineered tissues with complex geometries. Mater. Horizons 6, 1625–1631 (2019).

29. Qazi, T. H. & Burdick, J. A. Granular hydrogels for endogenous tissue repair. Biomater. Biosyst. 1, 100008 (2021).

30. O'Bryan, C. S., Kabb, C. P., Sumerlin, B. S. & Angelini, T. E. Jammed Polyelectrolyte Microgels for 3D Cell Culture Applications: Rheological Behavior with Added Salts. ACS Appl. Bio Mater. 2, 1509–1517 (2019).

31. Xu, Y. et al. Recent Advances in Microgels: From Biomolecules to Functionality. Small 18, (2022).

32. Graham, A. J. et al. MAGIC matrices: freeform bioprinting materials to support complex and reproducible organoid morphogenesis. bioRxiv 2024.02.01.578324 (2024).

CHAPTER 3: Pancreatic Ductal Adenocarcinoma Organoids Exhibit Pulse-Driven Collective Force Generation in Confinement

The subsequent section is adapted from a manuscript currently in review at the American Chemical Society Applied BioMaterials. Upon publication, all figures and data are subject to ACS Applied BioMaterials copyright.

Jonah M. Rosas*, Joseph P. Campanale*, Jacob L. Harwood, Rachel Bae, Shujun Cheng, Julia M. Tsou, Kathi M. Kaiser, Danielle D. Engle, Denise J. Montell, and Angela A. Pitenis

(*equally contributed to this work)

Abstract

Pancreatic ductal adenocarcinoma (PDAC) is a cancer of the epithelia comprising the ductal network of the pancreas. During disease progression, PDAC tumors recruit fibroblasts that promote fibrosis, increasing local tissue stiffness and subjecting epithelial cells to increased compressive forces. Previous in vitro studies have documented cytoskeletal and nuclear adaptation following compressive stresses in 2D and 3D. However, comparison of the responses of normal and tumor-derived ductal epithelia to physiologically relevant confinement remains underexplored, especially in 3D organoids. Here we control confinement with an engineered 3D microenvironment composed of Matrigel® mixed with a low yield stress granular microgel. Normal and tumor-derived murine pancreas organoids (normal and tumor) were cultured for 48 h within this composite 3D environment or in pure Matrigel® to investigate the effects of confinement on lumen morphogenesis. In confinement, tumor organoids (mT) formed lumen that expanded rapidly, whereas normal organoids (mN) expanded more slowly. Tumor organoids exhibited a collective "pulsing" behavior that increased in confinement. These pulses generated forces sufficient to locally overcome the yield stress of microgels in the direction of organoid expansion. Normal organoids more commonly exhibited unidirectional

rotation. Our in vitro microgel confinement platform enabled the discovery of two distinct modes of collective force generation in organoids that may shed light on dynamic collective cell behaviors.

1. Introduction

The microenvironment plays a key role in directing cell behavior during the onset and progression of diseases such as invasive breast carcinoma and pancreatic ductal adenocarcinoma. The protein composition and mechanical properties of the microenvironment, such as collagen type 1 abundance and tissue elastic modulus, have been correlated with invasive ductal epithelial cancers and poor clinical outcomes.[1–5] The tumor microenvironment facilitates disease progression by suppressing immune cell function,[6] imparting chemoresistance,[7] and establishing hypoxia.[8] During disease progression, the microenvironment dramatically stiffens due to infiltration of cancer-associated fibroblasts that locally deposit and align collagen type 1 in a process known as fibrosis.[6,9–12] Pancreatic ductal adenocarcinoma fibrosis results in collagen deposition that increases tissue stiffness and confines cells within the tumor microenvironment.[9,13] Cancer-associated fibroblasts contract and generate compressive stresses on cancer cells, confining tumors by maintaining tension along collagen fibers.[14]

PDAC is among the most fibrotic of epithelial cancers.[13,15] Although the extracellular matrix may initially constrain tumor growth, collagen proteins promote collective and mesenchymal invasion in vitro.[5,16] Studies have shed light on the adaptive mechanisms cancer cells leverage to navigate confined spaces in vitro, including altering cytoskeletal and nuclear deformability.[16–21] The extent to which cell morphology and collective behaviors are influenced by confinement is an active area of study. Confinement generally refers to the compressive stresses acting on cells as they squeeze through, deform, or proteolytically degrade narrow interstitial spaces that impede their migration

and/or growth.[22–24] 2D confinement studies have used rigid environments to investigate cellular response to confinement, but there are limited complimentary 3D systems to confine and support tissue-derived organoids in physiologically relevant mechanical niches. Organoid models exhibit structural similarities to their tissues of origin and help bridge the divide between 2D immortalized cell lines and in vivo organ development. Organoids offer an experimental system to investigate emergent collective cell behaviors that may contribute to disease progression.[25–30]

Here, we investigated the role of microenvironmental confinement on morphogenesis using tumor (PDAC) and normal murine-derived pancreas ductal organoids. We designed and implemented a 3D culture platform to create a "more confined" microenvironment using a low yield stress microgel support media compared to "less confined" Matrigel® encapsulation standards. Our results show that tumor organoids expand more rapidly than normal organoids under confinement. Furthermore, tumor organoids exhibit a "pulsing" behavior that increases in frequency in confinement and exerts force on the surroundings, suggesting pulsing allows tumors to rearrange the local microenvironment and expand. Together, these findings underscore the need for future investigations into collective force-generating behaviors in vitro and their physiological consequences in disease progression and metastasis.

2.0 Results

2.1 Microgels alter the spatial microenvironment

We investigated the effects of 3D confinement on pancreas organoid expansion and behavior using a low yield stress microgel platform with a tunable degree of confinement (Figure 1). Our system enabled real-time observation and measurement of

normal and tumor pancreas organoids in 3D. This microgel platform was composed of 3 wt.% polyacrylamide hydrogel microparticles

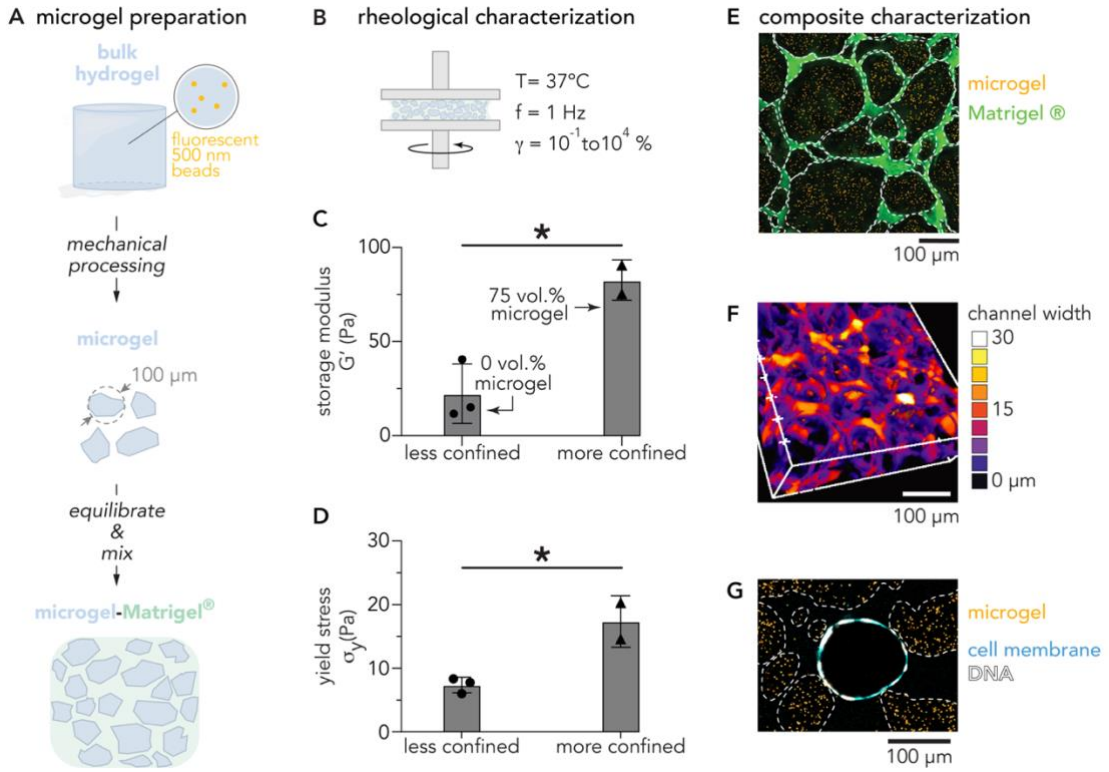
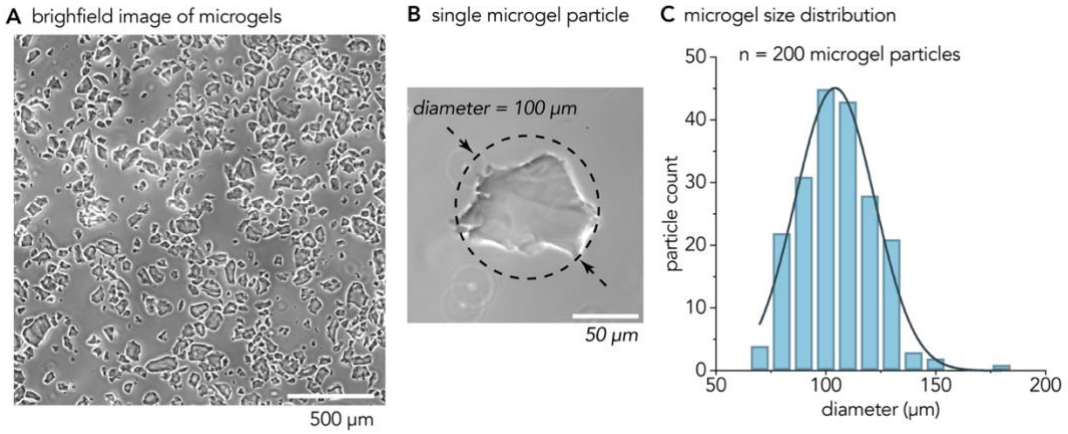


Figure 1 Microgel composites increase confinement. A) Illustration of microgel processing from bulk polyacrylamide hydrogel to 100 µm diameter microgels mixed with Matrigel® for organoid culture. **B**) Parallel plate rheometer geometry used to characterize microgel composite. **C**) Average storage modulus (G') for Matrigel® (less confined, n=3) and 75 vol.% microgel, 25 vol.% Matrigel™ composites (confined, n=2). **D**) Average yield stress of less confined (n=3) and confined (n=2) microenvironment. **E**) Confocal maximum intensity projection of confined microenvironment with FITC- Matrigel™ (green) and microgels labeled with orange polystyrene nanoparticles (diameter = 500 nm, particle concentration = 0.01 wt.%, Ex. 542 nm/Em. 612 nm). **F**) 3D heat map of channel width between microgel particles showing average channel width is 8 µm. **G**) Confocal maximum intensity projection of an organoid midplane. Organoid stained with CellTracker™ CMFDA (cytosol) and DNA (Hoechst 33342) with lumen in the center. Microgels embedded with orange fluorescent nanoparticles (diameter = 500 nm, particle concentration = 0.01 wt.%) and outlined with dashes. Statistical significance determined from unpaired t-test. *p ≤ 0.05. Error: SD. Scalebars = 100 µm.

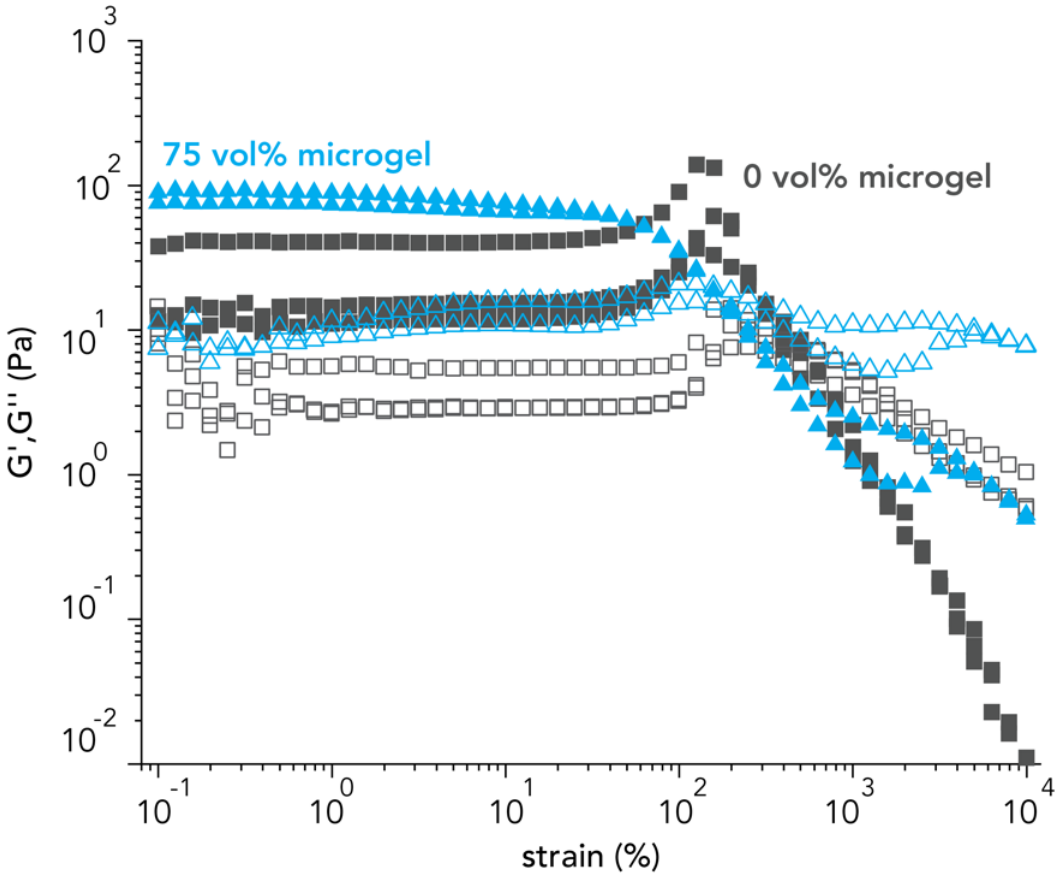
("microgels") of average diameter of 104 ± 17 µm S.D. (Supplementary Figure 1). Microgels were mixed with Matrigel® at a volume ratio of 75:25 microgel-to-Matrigel® (Figure 1A). We characterized the rheological properties of our microgel composite and 100% Matrigel® using a strain-controlled rheometer fitted with a parallel plate geometry

at physiological conditions, 37°C, 88% RH (Figure 1B). Storage modulus was evaluated across the plateau region at low strain (Figure 1C, Supplementary Materials 2).



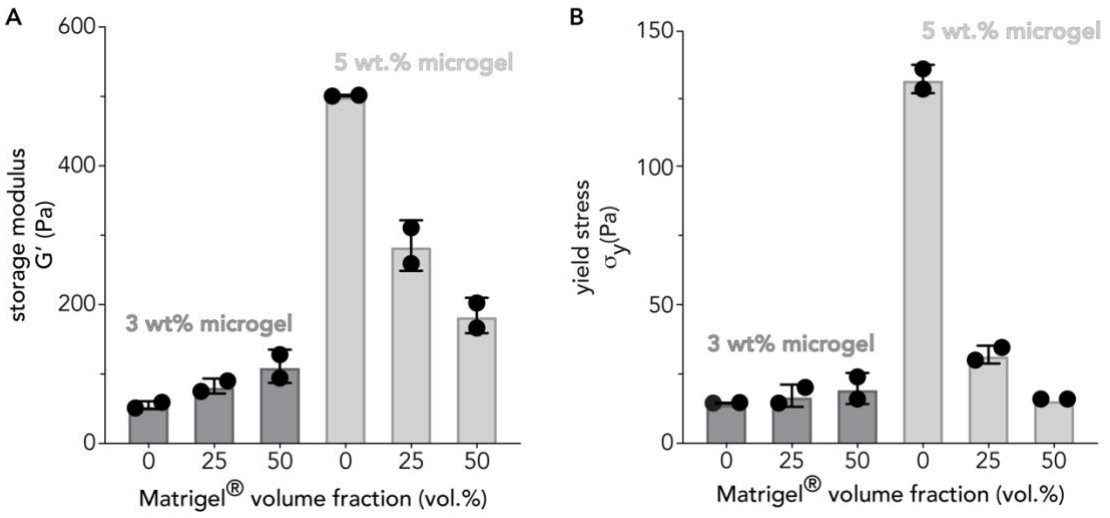
Supplementary Figure 1: Microgel particle sorting produces a narrow distribution of particle sizes Representative brightfield image of microgel particles used to determine average microgel size at **A**) low magnification 4× and **B**) high magnification 20×. **C**) Histogram of particle size distribution with average diameter of 104 ± 17 µm S.D for 200 measured particles.

Microgel composites had an average storage modulus of G' = 82.73 ± 10.76 Pa standard deviation, and Matrigel® had an average storage modulus of G' = 22.47 ± 15.78 Pa standard deviation. Yield stress (σ_y) was evaluated at the crossover of storage modulus, G', and loss modulus, G'', (Supplementary Materials 2, 3). Microgel composites had an average yield stress of σ_y = 17.35 ± 4.03 Pa standard deviation, and Matrigel® had an average yield stress of σ_y = 7.40 ± 1.22 Pa standard deviation (Figure 1C, D). Our microgel composite is stiffer and higher yield than Matrigel® alone, however, both materials are softer than normal tissue and tumors.[6] Such soft and low yield stress microenvironments allow for single cell growth and movement.[30–32]



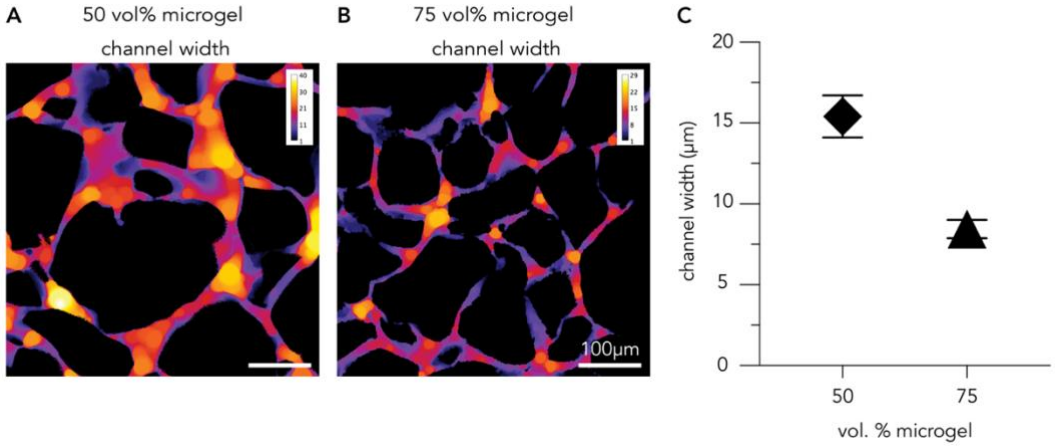
Supplementary Figure 2: Oscillatory strain rheology of less confined (Matrigel™, grey) and more. confined (75 vol.% microgel, blue) microenvironments. Storage modulus (filled circle and triangle) and loss modulus (open circle and triangle) at a frequency of 1 Hz, 37°C, and 88% RH.

To characterize confinement within the microgel composite, we measured the width of FITC-labeled Matrigel®(green) channels surrounding microgels (diameter ≈ 100 μm) containing a low concentration of fluorescent orange nanoparticles (diameter ≈ 500 nm) (Figure 1E). Microgel particles were surrounded by channels between 1 and 29 μm wide (Figure 1F). Channel width analysis showed an interconnected network of Matrigel® (lighter colors indicate wider regions; darker colors narrower) where the average channel width varied with microgel-Matrigel® volume ratios (Supplementary Figure 4).



Supplementary Figure 3: Rheological Properties of Microgel Composites Using Two Microgel Compositions. The **A**) storage modulus and **B**) yield stress of microgel composite systems generated using 3 wt.% (dark grey) and 5 wt.% (light grey) polymer content microgel particles. These data depict the distinct rheological properties that can be achieved by tuning both the polymer concentration of microgels and Matrigel® content within a composite system.

When microgel and Matrigel® were mixed in equal volume ratios, the channels were approximately 15 μm wide. Increasing the microgel-Matrigel® volume ratio to 75 vol.% reduced the average channel width to about 8 μm. Our microgel platform controls the proximity of passive hydrogel microparticles in 3D and controls confinement conducive for organoids to grow and undergo lumenogenesis (Figure 1G).



Supplementary Figure 4: Interstitial space between microgel particles narrows with increasing microgel volume fraction. Representative z-slices depicting A) 50 vol.% and B) 75 vol.% FITC-Matrigel™ channel

thickness represented as a heat map with cool blues depicting narrow regions and hot oranges depicting wide regions. C) Average channel widths for 50 vol.% (15.4 +/- 1.3 μm) and 75 vol% microgel (8.5 +/- 0.6 μm) were determined from a 500 μm × 500 μm ROI spanning 156 μm in z with a 2.2 μm step size. Organoids are generally larger than 100 μm in diameter. Error: SD.

2.2 Physical confinement constrains normal but not tumor organoid expansion

Confinement plays several roles in development and disease. The stromal compartment surrounding organs is an ECM-rich barrier that confines normal tissues during organogenesis.[31–35] The extracellular matrix undergoes compositional and geometric changes during disease transition that can impede or assist cancer metastasis.[21,36–38] Previous efforts have confined single cells in 2D using micropillars, rigid parallel plates, and other engineered systems[19], but platforms that similarly challenge organoids in 3D are underexplored. Our microgel platform presents an opportunity to impose compressive stresses on living organoids (Figure 1).

We cultured six independently isolated murine pancreas organoid lines,12 three normal (mN10, mN11, and mN12) and three tumor (mT8, mT9, and mT69A). Organoids were grown in two different confinement conditions: Matrigel® ("less confined") and microgel composite ("more confined") (Figure 2). After 48 h, we measured the outer organoid diameter at the midplane. As expected, tumor and normal organoids formed spherical monolayers surrounding a central lumen when grown in Matrigel® (Figure 2A, D) with tumor organoids expanding to larger final diameters than normal organoids (Figure 2 C, F and Supplemental Figure 4). Tumor organoids expanded to an average diameter d = 141.0 ± 81.40 μm S.D., while normal organoids expanded to d = 122.7 ± 60.66 μm S.D., which represents a roughly 10% difference.

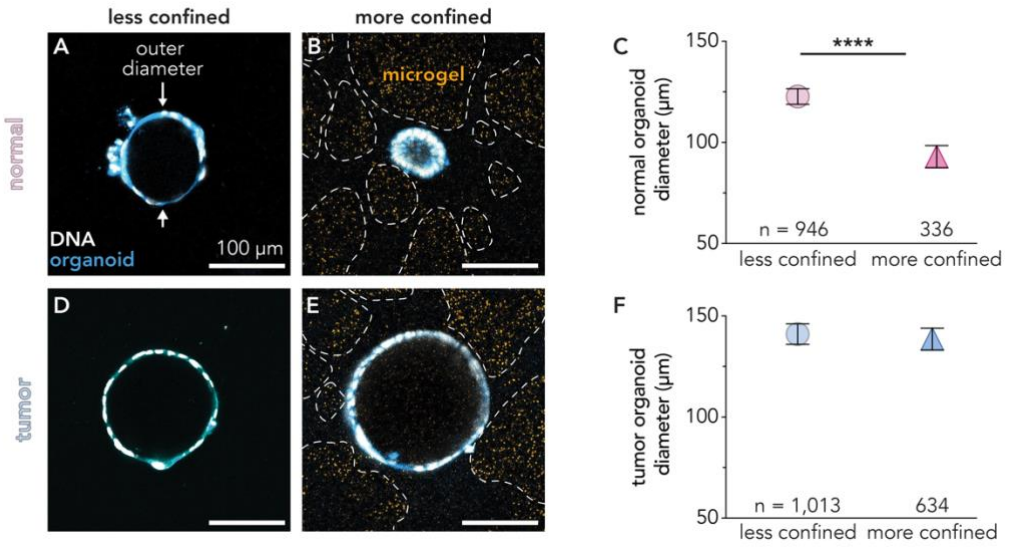
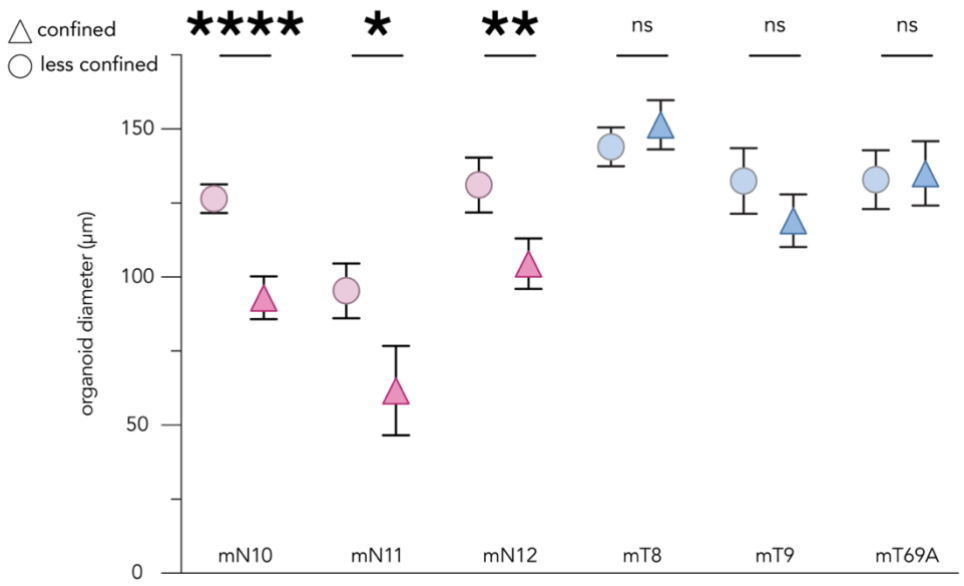


Figure 2 Organoids exhibit genotype-dependent sensitivity to confinement. A,B) Confocal images of organoid midplane stained with CellTracker CMFDA (cytosol) and DNA (Hoechst 33342) B) Microgels embedded with orange fluorescent nanoparticles (diameter = 500 nm, particle concentration = 0.01 wt.%) and outlined with dashes. C) Normal (mN) organoids have lower final diameter after 48 h when confined (pink triangle) than less confined (light pink circle). D,E) confocal images of tumors stained as in (A,B). F) Tumor (mT) organoids are similar sizes after 48 h when confined (blue triangle) and less confined (light blue circle). Statistical significance determined by Ordinary Two-Way ANOVA with Sidik's Multiple Comparison Test, with a single pooled variance. **** $p \leq 0.0001$. Error bars: 95% confidence intervals. Scalebars = 100 μm.

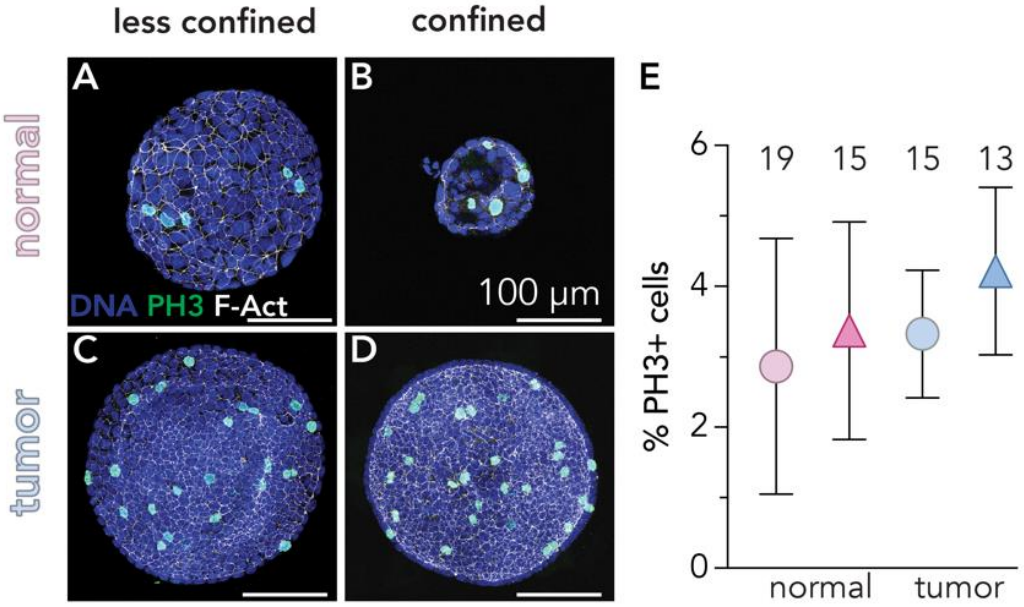
Surprisingly, both tumor and normal organoids expanded when confined by microgel particles in as little as 25 vol.% Matrigel®, although normal organoids expanded to smaller diameters when confined (Figure. 2A-B and Supplementary Figure 5). Normal organoids were approximately 24% smaller in more confined microenvironments than in less confined conditions. The average diameter of more confined normal organoids was d = 93.05 ± 51.09 μm S.D. while the average diameter in less confined conditions was d = 122.7 ± 60.66 μm S.D. (Figure 2C). In contrast, tumor organoids formed nearly identical average diameters across less confined and more confined microenvironments at d = 141.0 ± 81.40 μm S.D. and d =138.5 ± 69.41 μm S.D., respectively (Figure 2D-F). Normal organoids were about 13% smaller in diameter than tumor organoids in less confined microenvironments and approximately 33% smaller in more confined microenvironments.



Supplementary Figure 5: Normal organoids sensitivity to confinement while tumor organoids do not. Normal (mN) organoids in confined (pink triangles) microenvironments grew to smaller diameters than in less confined (light pink triangles) microenvironments after 48 h (N=3 biological replicates, n ≥ 49 organoids measured). Tumor (mT) organoids in confined (blue triangles) microenvironments grew to similar diameters as in less confined (light blue circles) microenvironments after 48 h (N=3 biological replicates, n ≥ 49 organoids measured). Statistical significance was determined using an Ordinary Two-Way ANOVA with Sidik's Multiple Comparison Test, with a single pooled variance. *p ≤ 0.05,**p ≤ 0.01, **** p ≤ 0.0001.

2.3 Confinement disrupts apico-basal polarity in normal organoids

Epithelial tissues and organoids expand through cell division and/or cell shape change. Given that confined microenvironments constrain the expansion of normal but not tumor-derived organoids, we tested whether effects on cell division might account for the different responses to confinement. We quantified division by measuring the number of phospho-histone 3 expressing (PH3+) cells per organoid (Supplemental Figure 5).



Supplementary Figure 6: Cell division in normal and tumor organoids. A-D) Normal (**A**,**B**) and tumor (**C**,**D**) organoids grown in less confined and confined environments for 48 hours. Dividing cells marked with phospho-histone3 (PH3, green). DNA stained with Hoescht (blue) and F-acting with phalloidin (gray). **E**) Quantification for the percentage of PH3 positive cells. Number of organoids counted above each symbol with confidence intervals. Scale bars 100 µm.

When normalized to the total number of cells per organoid, normal organoids underwent cell division at similar rates in less confined (Supplemental Figure 5A) and more confined (Supplemental Figure 5B) microenvironments. Similarly, we found no significant differencecell division for tumor organoids in less confined (Supplemental Figure 5C) and confined (Supplemental Figure 5D) microenvironments. Thus, normal and tumor organoids divide at similar rates regardless of a confining microenvironment (Supplementary Figure 6).

Changes in cell shape can also drive morphogenesis, including the formation of luminal organs.[39] Pancreatic organoids grown in Matrigel® organize into a single layer of columnar epithelial cells with apical membranes facing an internal lumen, lateral membranes between cells, and basal membranes touching the extracellular matrix.[40] After establishment of polarity, changes in cell shape accompany increasing organoid diameters. Tall, columnar cells transition to short and flat squamous morphology while

retaining apical-in (lumen-facing) polarity. All normal organoids grown in 100% Matrigel® transitioned from columnar into squamous cells with apical membranes containing atypical protein kinase C (aPKC), an apical determinant, facing toward the lumen and Scribble, a basolateral determinant, between cells (Figure 3A-A', C). However, 62% of normal organoids grown in more confined environments exhibited inverted apicobasal polarity (Figures 3B-C). aPKC positive membranes were facing the Matrigel®-microgel composite, and basolateral membranes faced inwards to small lumens. Tumor organoids grown in both less and more confined conditions had indistinguishable diameters and were composed of flat squamous cells with aPKC-positive membranes facing central lumens (Figures 3D-E').

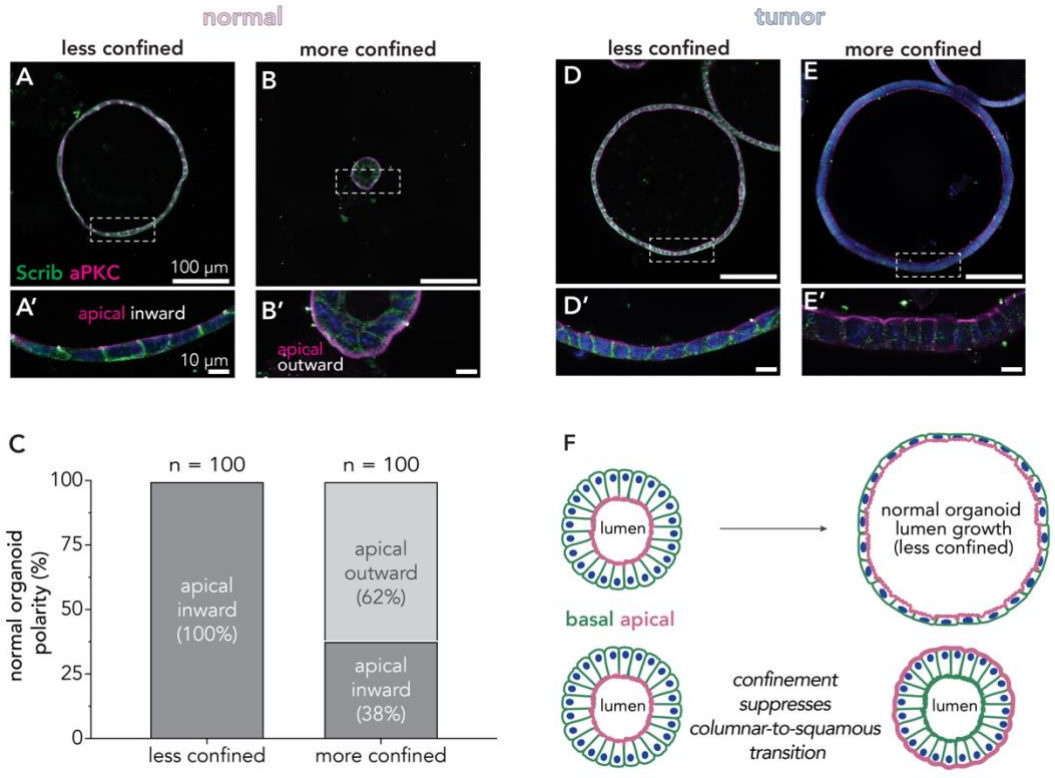


Figure 3 Confinement disrupts cell polarity and inhibits columnar-to-squamous transition in normal organoids. A,B) Confocal images of murine normal organoids grown in less confined **A**) and confined **B**) conditions and stained for the basolateral membrane marker Scribble (green) and the apical marker aPKC (magenta) and DNA in blue. **A',B'**) zooms of the insets in **A,B. C**) Percentage of organoids exhibiting normal polarity with apical membranes interfacing inward toward the lumen, or with apical membranes facing outward toward the extracellular environment. **D-E'**) Confocal images of murine tumor organoids stained as

in **A-B'**. **F**) Illustration of apical and basal membranes as cells transition from columnar to squamous during normal lumen volume increase.

Thus, the apical inward polarity of normal organoids (Figure 3F) is disrupted when more confined. In contrast, confinement had no effect on tumor organoid morphogenesis. Taken together, we conclude that confinement suppresses normal organoid lumen expansion in part by preventing the columnar-to-squamous transition and inverting apicobasal polarity.

2.4 Confinement slows normal but not tumor organoid expansion

An advantage of organoid models over in vivo mouse studies is the ability to observe morphogenesis in real time. Leveraging this, we used time lapse imaging to characterize normal and tumor organoid lumen expansion kinetics in less confined and more confined conditions over 48 h using Differential Interference Contrast (DIC) microscopy (Figure 4, Supplementary Movies 1-4). Normal organoids expanded linearly in Matrigel® (Figure 4A, A'). Tumor organoid expansion was punctuated by striking rapid contractions followed by whole organoid re-expansion (Figure 4B, B'). We defined a contraction events or "pulses" by a loss in organoid area exceeding 10%. In contrast, normal organoids did not exhibit the same pulsing behavior. Organoid expansion rates were visualized by plotting organoid cross-sectional area as a function of time (Figure 4C, D*, Supplementary Figure 7*). The steeper the slope, the faster the change in organoid expansion. Representative plots of a single normal organoid's projected area over time indicated faster expansion in less confined (light pink circle) than in more confined (pink triangle) conditions (Figure 4C). Representative plots of a single tumor organoid tracked over 48 h exhibited multiple pulses labeled in Figure 4D. In contrast to normal *organoids*, tumor organoid expansion kinetics were largely insensitive to confinement. Interestingly, the number of pulses increased in more confined conditions (Figure 4D). Normalized area measurements of many organoids showed normal (light pink circle, n=43) and tumor (light blue circle, n=57) organoids expanded at similar rates in less confined microenvironments with tumors expanding slightly faster (Figure 4E). These data were consistent with the observation that tumor organoids were larger than normals after 48 h in less confined environments (Figure 2G). Tumor organoids (blue triangle, n=45) expanded faster than normal organoids (pink triangle, n=20) in more confined conditions (Figure 4F). Tumor organoids maintained similar area fold changes in both microenvironments. Together, these results suggest normal organoids expand slower when confined, while tumor organoids continue expanding despite confinement.

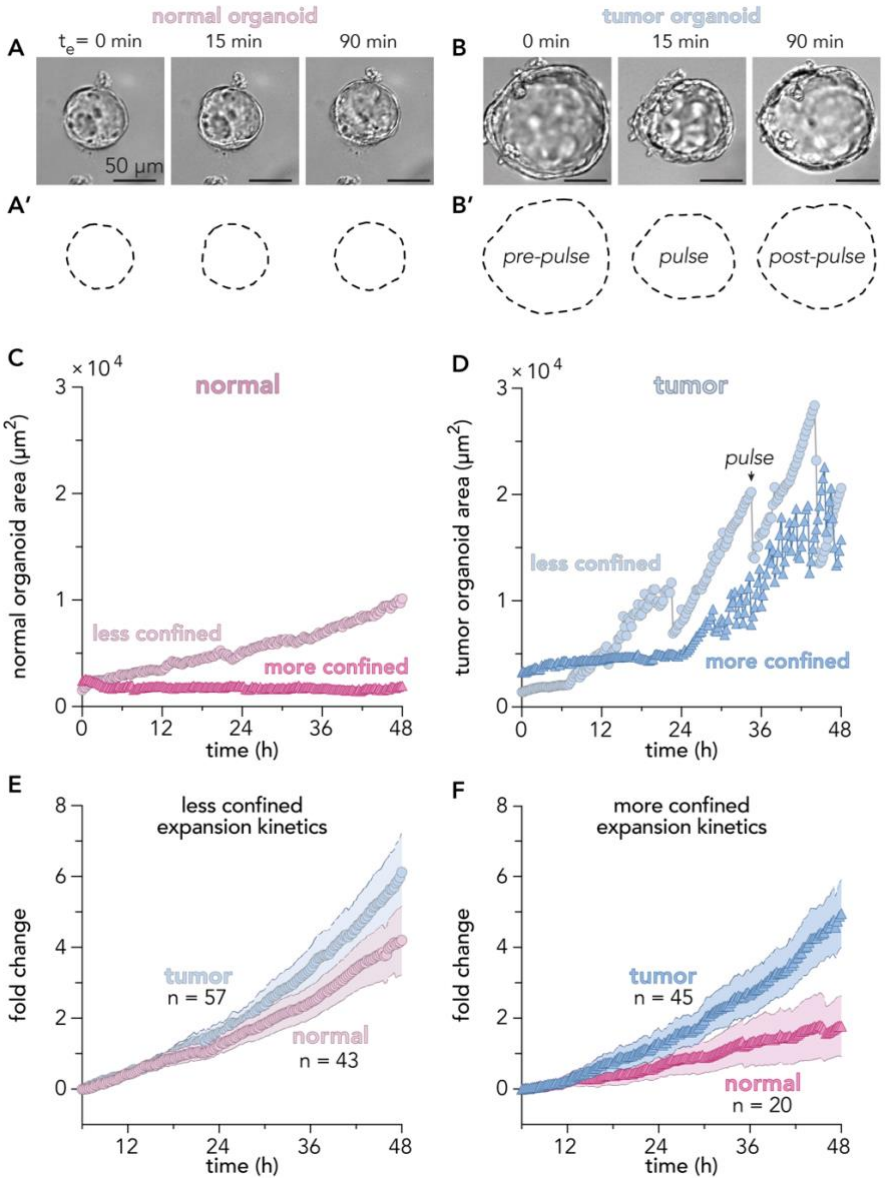
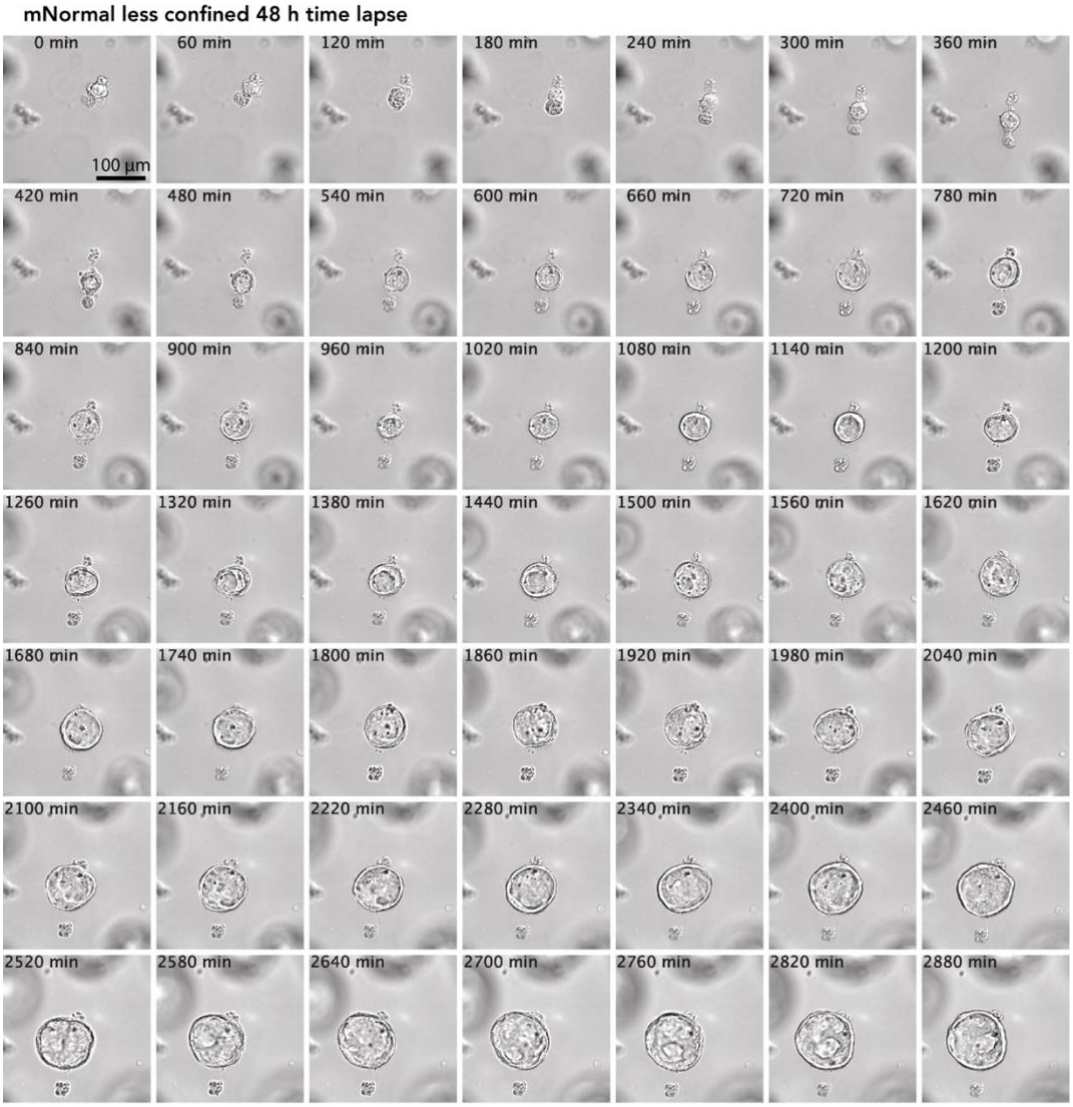
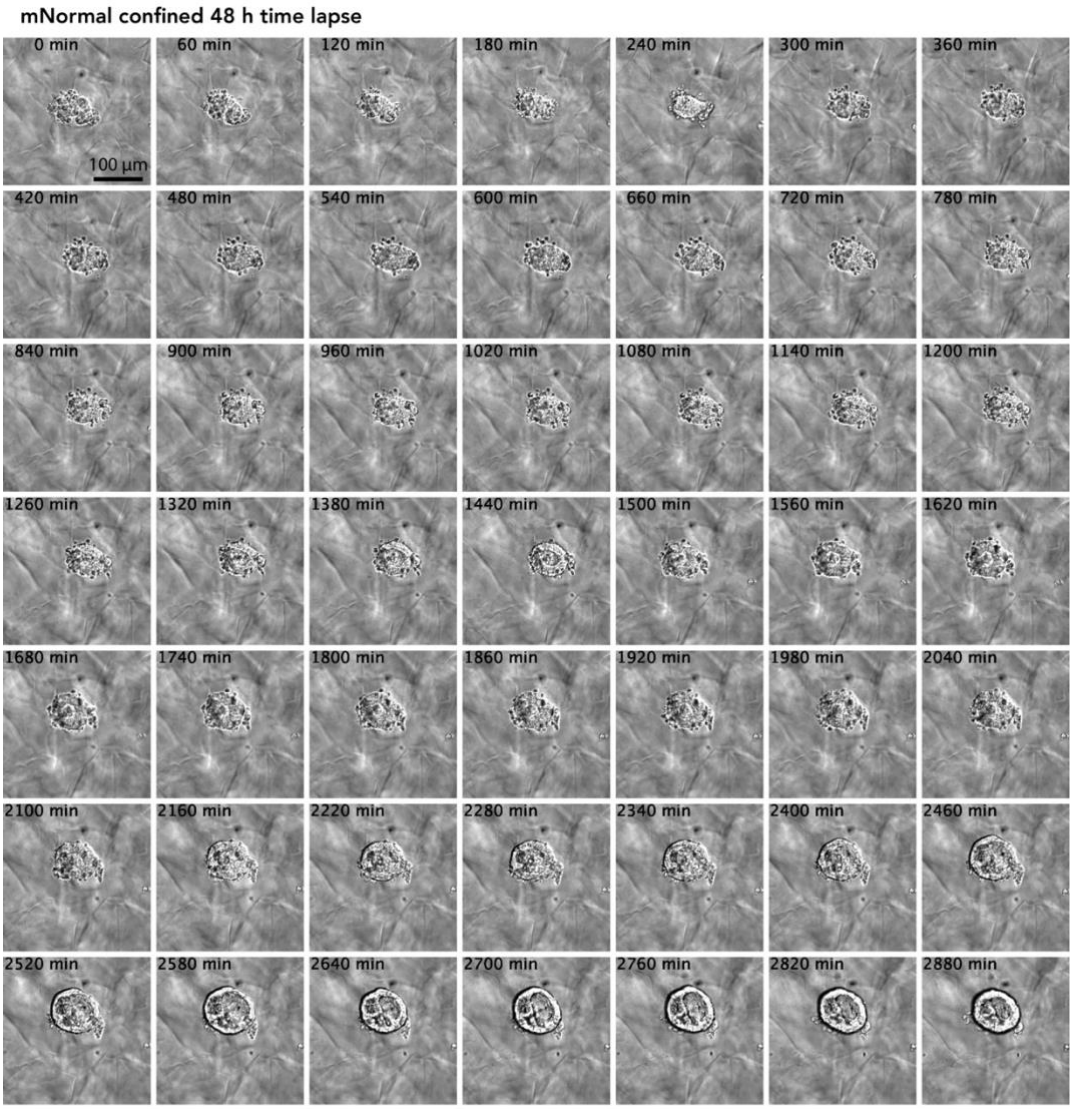


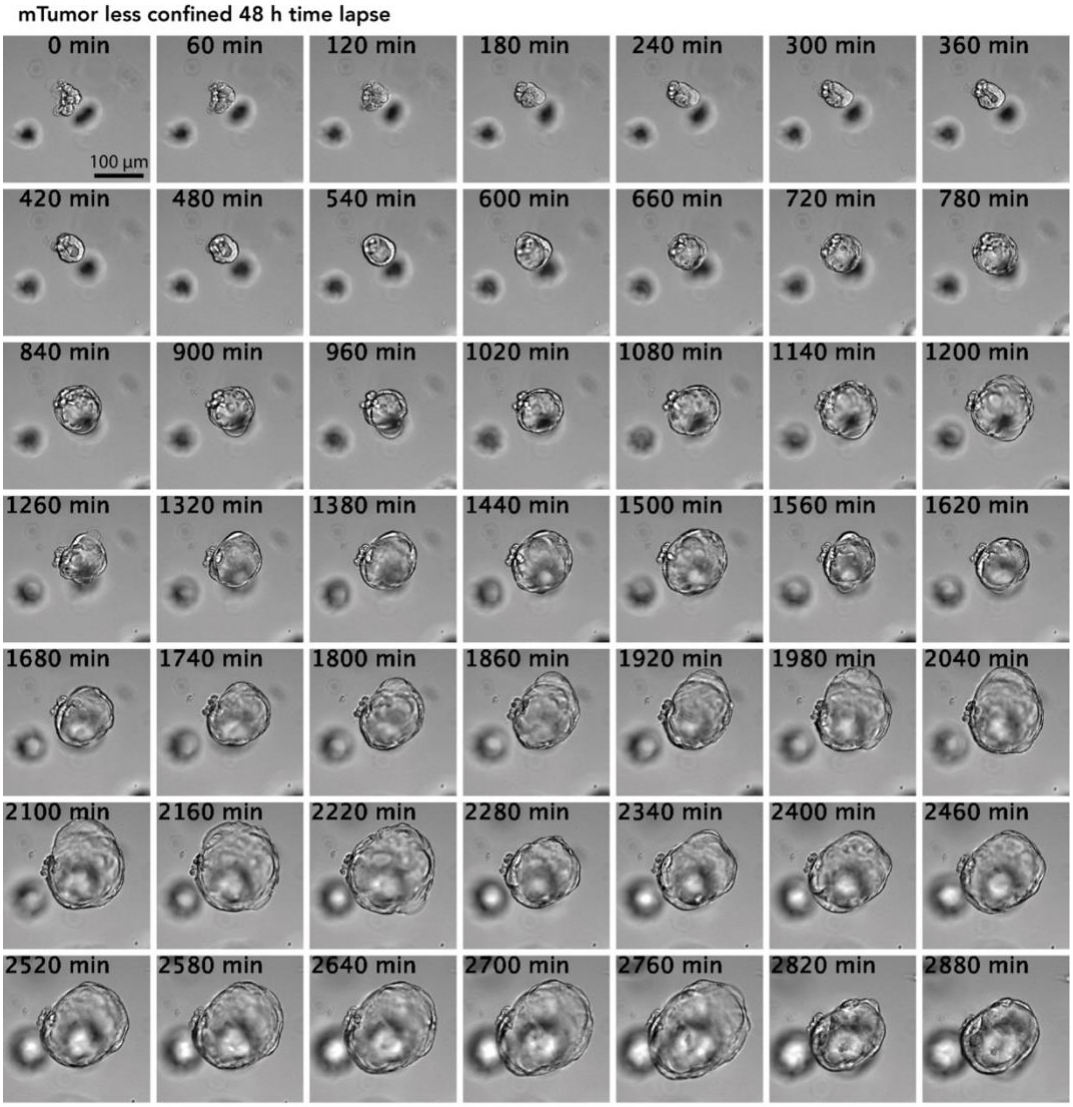
Figure 4 Organoid projected area and expansion kinetics over time. A) Normal organoids expand linearly with limited area fluctuations between 15 min acquisitions shown in DIC imaging and A') projected area traces. B) Tumor organoids undergo rapid expansion, collapse or "pulse" (< 15 min), and re-expansion (< 90 min) shown in DIC imaging and B') projected area traces. Here, a pulse is defined as an organoid contraction with an area loss >10% within 15 min. C) Organoid area profiles for normal (mN) organoids in less confined (light pink circle) and confined (pink triangle) microenvironments (n=1). D) Organoid area profiles for tumor (mT) organoids in less confined (light blue circle) and confined (blue triangle) microenvironments (n=1). E) Average population expansion kinetics profiles for mN (light pink circle, n=43) and mT (light blue circle, n=57) organoids in less confined microenvironment. F) Average population expansion kinetics profiles for mN (pink triangle, n=20) and mT (blue triangle, n=45) organoids in confined microenvironment. Scale bars = 50 µm. Error: 95% confidence interval.



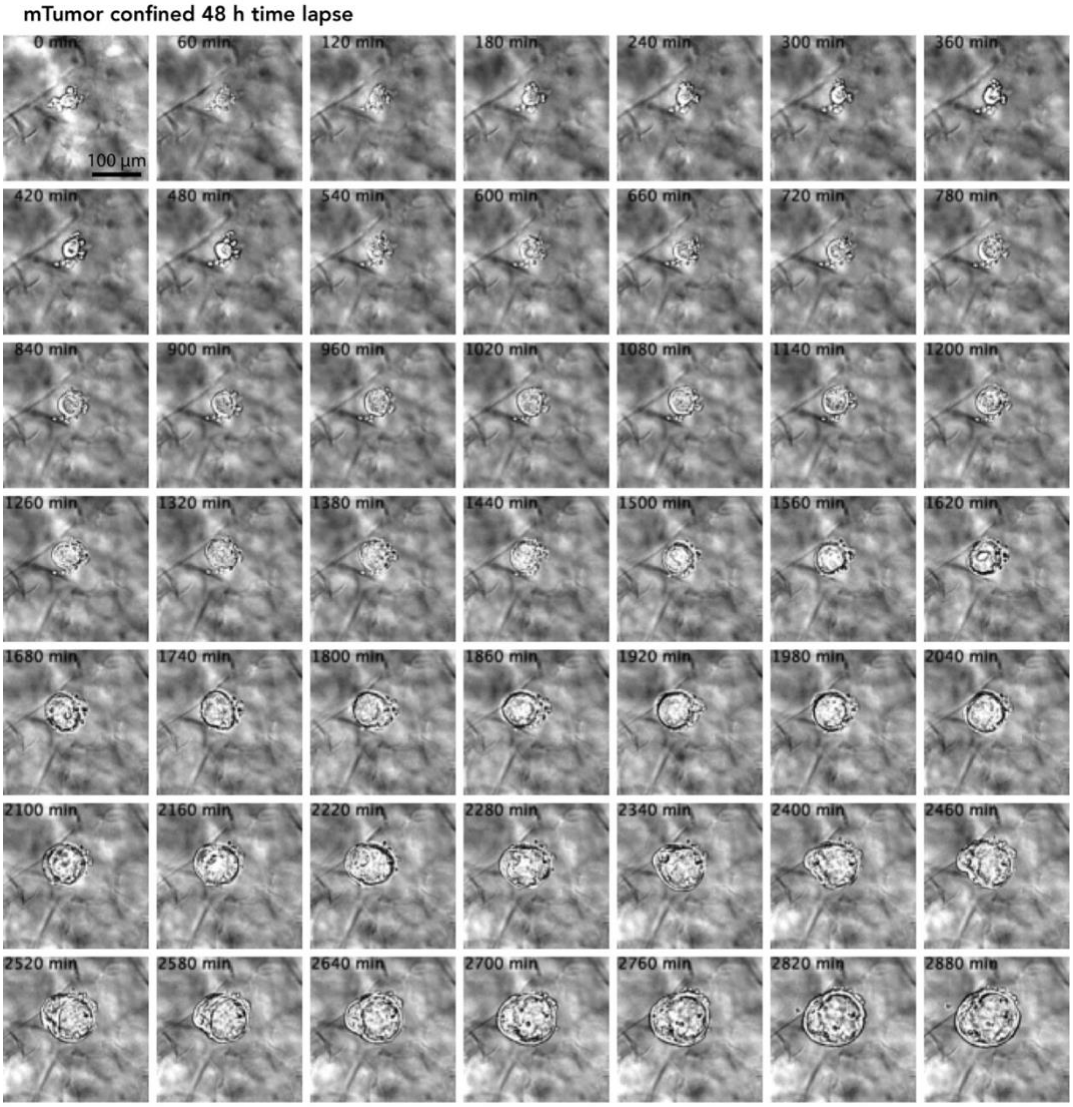
Supplementary Movie 1: DIC time lapse of normal organoids expanding in less confined microenvironment. Tiles depict every 60 min of a 48 h timelapse with acquisitions every 15 min. Scalebar = 100 µm.



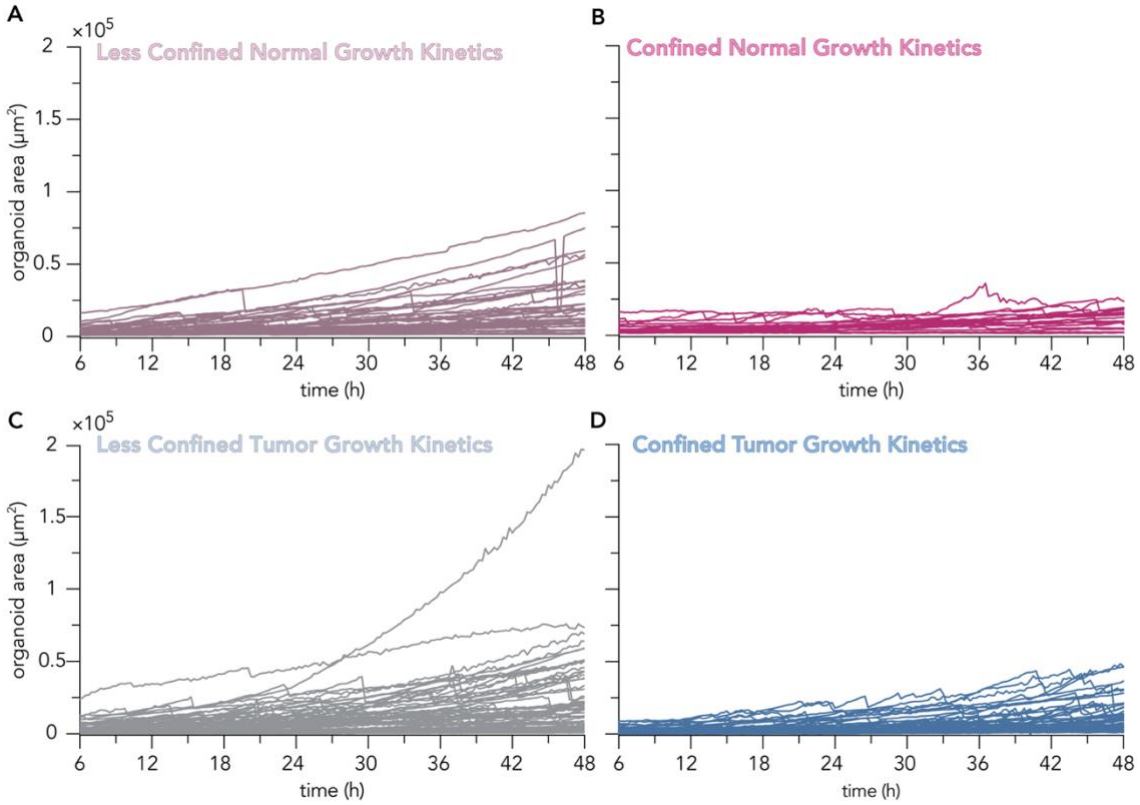
Supplementary Movie 2: Time lapse of normal organoids expanding in confined microenvironment. Tiles depict every 60 min of a 48 h timelapse with acquisitions every 15 min. Scalebar = 100 µm.



Supplementary Movie 3: Time lapse of tumor organoids expanding in less confined microenvironment. Tiles depict every 60 min of a 48 h timelapse with acquisitions every 15 min. Scalebar = 100 µm.



Supplementary Movie 4: Time lapse of tumor organoids expanding in confined microenvironment. Tiles depict every 60 min of a 48 h timelapse with acquisitions 15 min. Scalebar = 100 µm.



Supplementary Figure 7: Organoid growth kinetics. Multiple organoid area traces for A) normal organoids in less confined microenvironment (n = 43), B) normal organoids in confined microenvironment (n = 20), C) tumor organoids in less confined microenvironment (n = 57), and D) tumor organoids in confined microenvironment (n = 45).

2.5 Tumor organoids move nearby microgel particles in the direction of expansion

Pulsing tumor organoids may generate stresses sufficient to locally yield the microenvironment. We investigated how organoids physically interact with their microenvironment during expansion by embedding fluorescent tracer particles (500 nm diameter) in microgel (Figure 5A) in more confined conditions. Well-spaced organoids were selected for imaging to eliminate particle movements due to nearby organoids. Particle trajectories revealed distinct organoid-microgel interactions for normal and tumor organoids. Normal organoids rotated, spinning adjacent microgels opposite the direction of organoid rotation(Figure 5B, B'). Normal organoid rotations were consistent with recent reports of collective rotation in murine pancreas-derived organoids.[41]

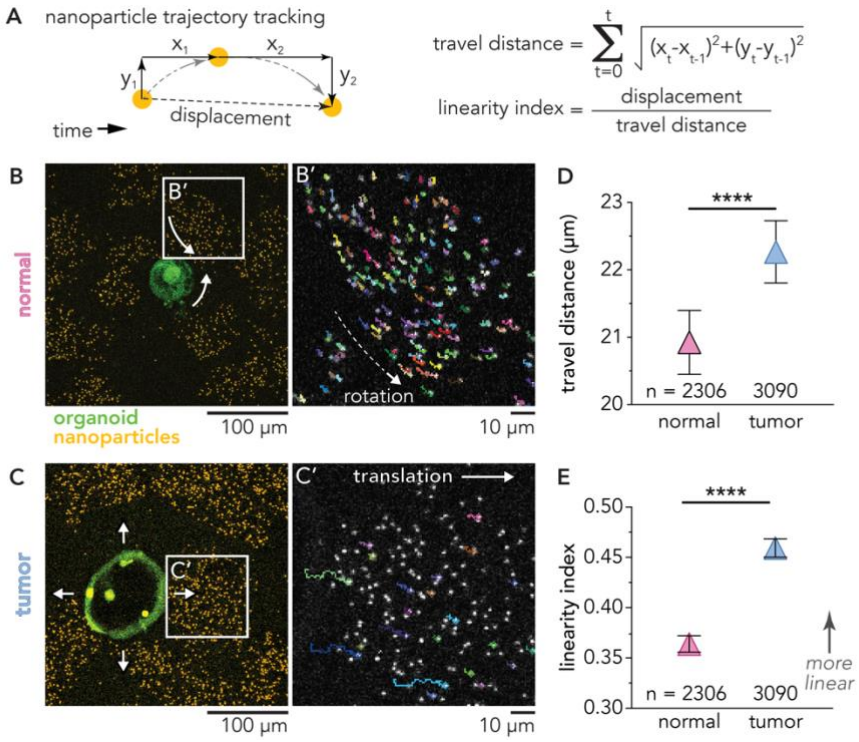


Figure 5 Particle tracking quantifies microgel displacement due to organoid movement. A) Schematic of single particle tracking with travel distance and linearity index defined. **B**) Normal organoid in confined microenvironment generates **B'**) rotational trajectories. **C**) Tumor organoid in confined microenvironment generates **C'**) linear trajectories. Particle trajectory **D**) travel distances and **E**) linearity indices (normal : n = 2,306 trajectories, N = 13 organoids; tumor: n = 3,090 trajectories, N = 17 organoids). Statistical significance determined using unpaired t-test. **** $p \leq 0.0001$. Error bars: 95% confidence intervals. Scale bar = 100 µm for composites, 10 µm for inset.

Tumor organoids, in contrast, did not exhibit significant rotation but pulsed linearly outward against the surrounding microenvironment during expansion (Figure 5C, C'). Over the same 24 h period, tumor organoids moved microgels further (Figure 5D) and with a more persistent direction. The ratio of particle displacement (end-to-end distance) to total distance traveled was defined as the linearity index, or the persistence of a particle's trajectory. Thus, more straighter tracks have a higher linearity index. Analysis of normal (pink triangle) and tumor (blue triangle) organoid linearity confirmed that tumor organoids generated straighter tracks during expansion (Figure 5E). Thus, in confinement, the ability to exert force in the direction of expansion may facilitate tumor growth.

2.6 Tumor organoids increase pulse frequency under confinement

Tumor organoids pulsed more frequently in confined conditions (Figure 4D), suggesting confinement induces pulsing. We measured change in organoid cross-sectional area every 15 min for 48 h (Figure 6A-D) to quantify organoid pulse rates. Negative area change indicated rapid contraction, whereas positive area change indicated rapid expansion. Single organoid pulse profiles highlighted differences between normal and tumor organoids. Whereas normal organoids seldom pulsed in either less confined (Figure 6A) or more confined conditions (Figure 6B), tumor organoids pulsed in less confined conditions (Figure 6C) and increased pulse frequency in more confined conditions (Figure 6D, E).

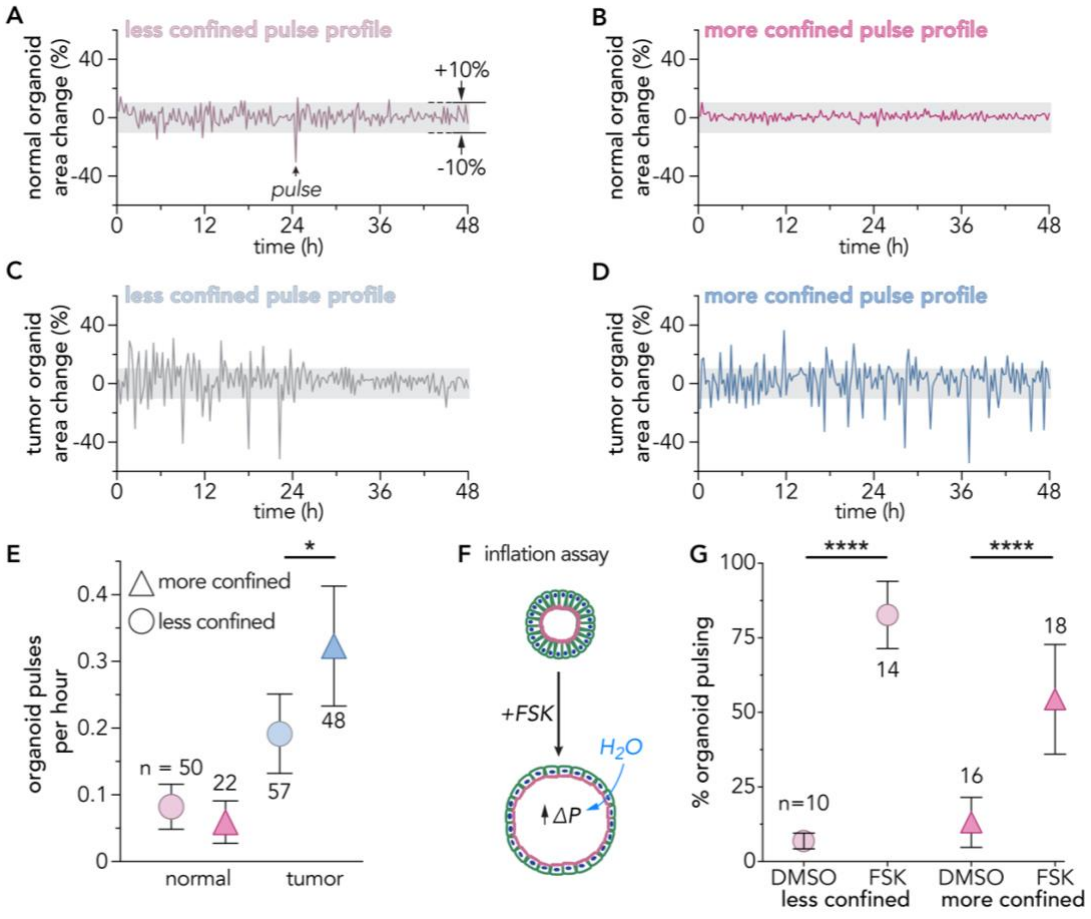
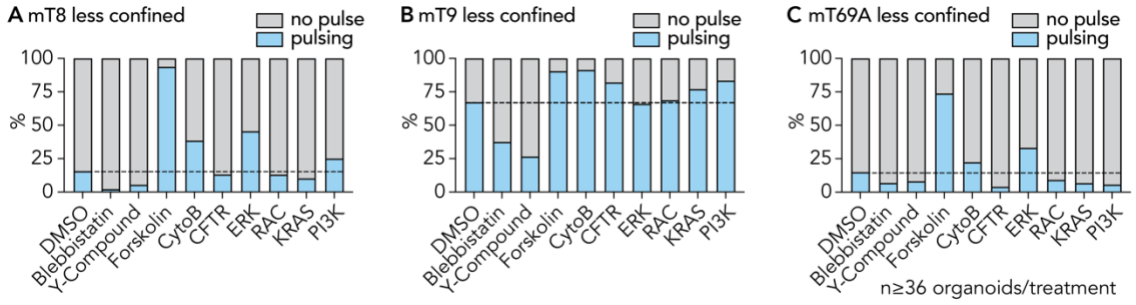


Figure 6 Tumor and normal organoid pulse profiles. A) Pulse profiles of a normal organoid every 15 minutes in unconfined and B) confined environments. C) Pulse profile of a tumor organoid every 15 minutes in unconfined and D) confined environments. A pulse is defined as an organoid contraction with an area loss >10% within 15 min, and the grey bounding box indicates +/- 10% area change. E) Normal and tumor pulse rate (pulses per hour) in less confined (circle) and confined (triangle) microenvironments with mean

pulse rate and 95% confidence interval. F) Schematic of an organoid inflation assay caused by a forskolin (FSK) dependent increase in lumen hydrostatic pressure. G) The percent of normal organoids per field of view that pulse in less confined (circles)(n_{DMSO} = 10, n_{FSK} = 14) and confined (triangles)(n_{DMSO} = 16, n_{FSK} = 18) microenvironments with mean pulse rate and 95% confidence interval. Statistical significance was determined using an Ordinary Two-Way ANOVA with Sidik's Multiple Comparison Test, with a single pooled variance. *$p \leq 0.05$, **** $p \leq 0.0001$.

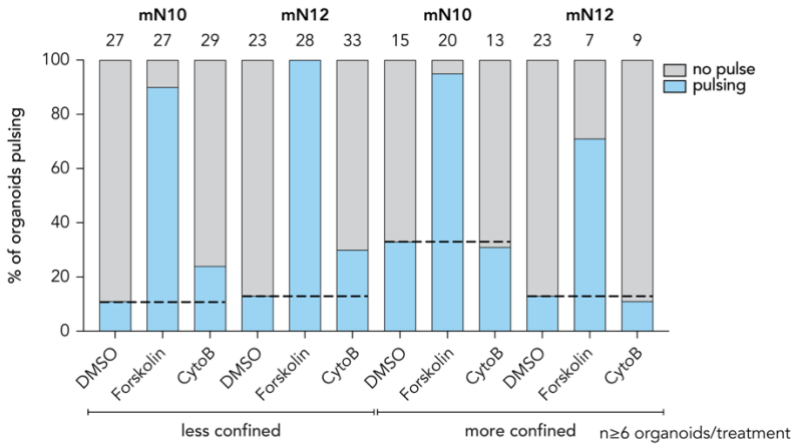
To investigate the cellular mechanisms driving expansion and pulsing, we performed a pharmacological screen targeting lumen hydrostatic pressure (forskolin), cytoskeletal assembly and dynamics (blebbistatin, y-compound, cytochalasin B), and several signaling pathways (MRTX-1133, VX-11e, wortmannin) (Supplementary Figure 8). Out of 8 independent drug treatments, forskolin (FSK) provided the most consistent and largest effect, increasing the percentage of pulsing tumor organoids in a less confined microenvironment (Supplementary Figure 8).



Supplementary Figure 8: Percentage of tumor organoids pulsing when treated with 8 small molecules targeting cytoskeletal elements, ion channels, and signaling pathways. Para-amino-Blebbistatin is an inhibitor of non-muscle myosin II ATPases that rapidly and reversibly targets the activity of non-muscle myosin II A and B. Y-27637 Hydrochloride (y-compound) is a rho kinase inhibitor that target ROCK-I and ROCK-II. Forskolin is a cAMP activator that increases chloride ion transport and water flux in the apical direction. Cytochalasin B is a actin assembly inhibitor, preventing the formation of a dense actin network necessary for contractility.CFTR(inh)-172 is a potent and selective CFTR chloride ion channel blocker, preventing apical fluid secretion. VX-11e is a selective ERK2 inhibitor. ETH-1864 is a selective Rac GTPase inhibitor blocking activation through direct binding to Rac1 Rac 1b, Rac2, and Rac3.MRTX-1133 is a selective $KRAS^{G12D}$ inhibitor that targets the hyperactive form of KRAS found mutated in the KPC organoid models used in this study. Wortmannin is a selective and irreversible PI3K inhibitor. Greater detail on drug mechanisms can be found in manufacturer specifications.

Forskolin increases cAMP levels, which results in the opening of cystic fibrosis transmembrane conductance regulator (CFTR) channels and has been used to stimulate organoid swelling (Figure 6F).[42] The dynamics of lumen inflation and collapse are well known to rely on CFTRs.[43] Therefore, we assessed whether increasing luminal pressures

with forskolin could induce normal organoid pulsing in each confined condition. Forskolin treatment increased the percentage of pulsing normal organoids in both less confined and more confined environments (Figure 6G, Supplementary Figure 9). Taken together, these data demonstrate that tumor organoids pulse more frequently in more confined environments, and normal organoids will begin pulsing in response tin increased hydrostatic pressure.



Supplementary Figure 9: Forskolin induces pulsing in normal organoids Percentage of normal organoids pulsing in less confined and more confined conditions when treated with forskolin and cytochalasin B.

2.7 Increased hydrostatic pressure partially rescues normal organoid apico-basal polarity but not size in confinement

Epithelial cells must regulate hydrostatic pressure for lumen inflation.[43,44] We found that pancreatic tumor organoids pulsed more frequently when confined and maintained normal apicobasal polarity whereas normal organoids pulsed less and often reverse polarity (Figure 6). Since forskolin induced normal organoid pulsing, we hypothesized pulsing may assist in maintaining normal organoid polarity and organoid size in more confined conditions. Normal organoids in less confined conditions had proper apical inward aPKC localization in both DMSO (Figure 7A, A') and forskolin treatments (Figure 7B, B').

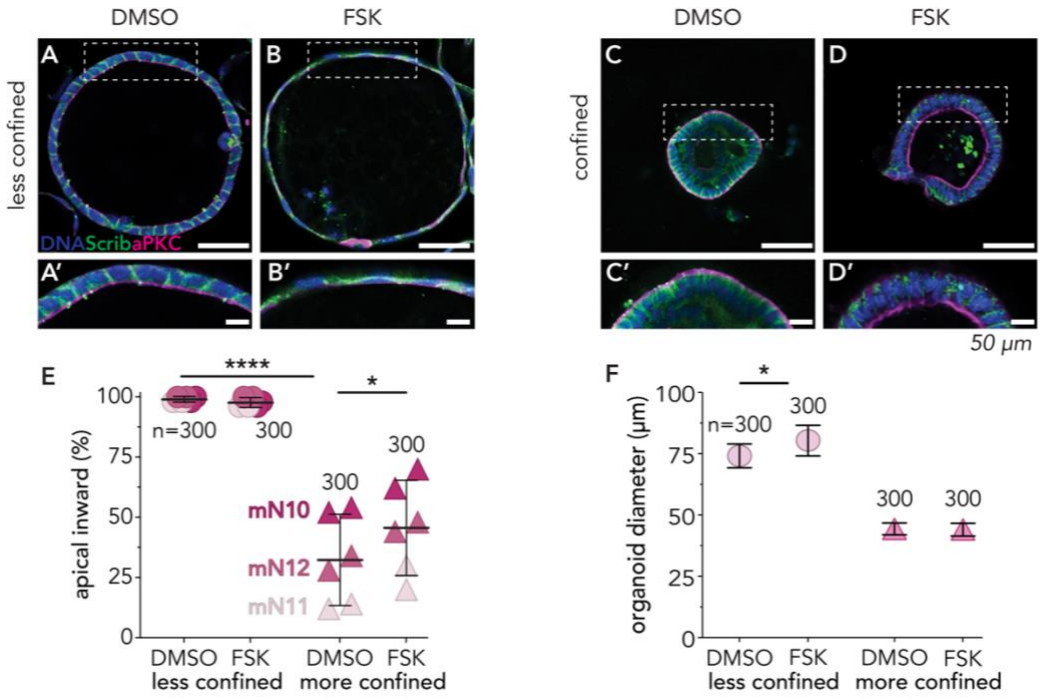


Figure 7 Increased hydrostatic pressure partially rescues normal organoid polarity but not size. A) DMSO-treated normal organoid polarity in less confined microenvironments stained for SCRIB at basolateral surfaces and aPKC at apical membranes. **A')** zoom of boxed region in A. B) Forskolin-treated normal organoid polarity in confined microenvironment stained as in A and zoomed as in A' C-D') Normal organoids grown in the confined condition, and treated and stained as A-B'. E) Quantification of percent normal organoids with apical membranes facing inward toward lumen. F) Normal organoid diameter measurements at 48 h in less confined (circles) and confined (triangles) after treatment with DMSO or Forskolin. Error: 95% CI. All statistical significance determined using ANOVA. In E, the factors the two-way ANOVA were cell-line and treatment with a Tukey post-hoc analysis. *$p \leq 0.05$,**$p \leq 0.01$, ***$p \leq 0.001$, **** $p \leq 0.0001$. Scale bar = 50 μm.

In contrast, normal organoids in more confined conditions had inverted apical outward aPKC staining (Figure 7C, C') that was partially reverted to apical inward aPKC staining with forskolin treatment (Figure 7D, D'). Forskolin treatment improved the population of organoids with proper apical inward polarity by ≈ 12% but was insufficient to restore normal organoid size after 48 h (Figure E, F).

3.0 Discussion

The *in vivo* tissue microenvironment is a multi-component system composed of functional communities of cells surrounded by an extracellular matrix. During PDAC disease progression, cancer associated fibroblasts deposit and remodel the extracellular matrix,

generating compressive stresses upon normal and cancer cells[1,20,37,46–48]. In colorectal cancer, compressive stresses restrict cancer growth while also complicating therapeutic interventions by collapsing blood vessels.[49] Here, murine pancreas ductal organoids derived from normal and PDAC tissues were confined using a 3D low yield stress platform that modulated the rheology of Matrigel®. Our engineered microenvironment allowed us to confine organoids and compare normal and tumor organoid responses to confinement.

The expansion of epithelial tissues typically occurs in one of two ways: (1) by adding cells through division or (2) rearrangement of existing cells through processes such as convergent extension, intercalation, or columnar-to-squamous transition[50–52]. Although confinement did not affect cell division rates in either normal or tumor organoids (Supplementary Figure 6), we determined that normal organoids – but not tumor organoids – failed to undergo columnar-to-squamous transitions in confinement and instead exhibited inverted, apical-outward polarity. Tumor organoids, in contrast, are known to display irregular polarity patterns, which may contribute to their ability to overcome confinement and regulate hydrostatic pressure. Hydrostatic pressure increases occur by the secretion of ions, accompanied by the movement of water into a lumen. Multiple mechanisms regulate hydrostatic pressure during development and morphogenesis, including: fluid release by basal valve-like lamellae, fissures in cell junctions leading to paracellular movements of water by hydraulic fracturing, or the stretching of cells into more squamous morphology.[45,54,56] The exocrine secretion function of the pancreas requires ion-dependent fluid secretion and these channels are aberrantly expressed and mislocalized in PDAC.[57,58] How tumors utilize ion fluxes and pulsing to grow in confined environments, and whether normal tissues more tightly regulate intraluminal pressures *in vivo* remain open questions and warrant further investigation.

Notably, we observed that tumor organoids pulsed more frequently when confined, which raised the question whether pulsing confers an adaptive advantage. Collective pulsing has been reported in patient-derived ovarian cancer spheroids,[53] normal murine pancreas organoids,[26] and mammalian embryos,[54] but there remain limited investigations into how pulse rates differ between normal and cancerous tissues and how pulsing is altered by confinement.[26,53] Tumor-derived, pancreas organoid pulsing has not been examined until now. The observation of collective pulsing across human ovarian spheroids, murine pancreas ductal organoids, and mammalian embryos suggests it may be a general feature of cystic epithelia.[55]

Live imaging of healthy and tumor organoids at different levels of confinement revealed changes in organoid expansion kinetics and dynamics. We discovered collective pulsatile and rotational behaviors that generated forces on the surrounding microenvironment. The emergent pulsing behavior in PDAC organoids correlated with organoid expansion under confinement, whereas the rotational behavior of normal organoids was correlated with slowed expansion kinetics under confinement. We further demonstrated pulsing could be induced in normal organoids treated with forskolin, but pulsing alone was insufficient to fully rescue normal organoid diameter and native apicobasal polarity. Thus, there must exist multiple features of luminal pressure regulation that differ between normal and tumor organoids that warrant further investigation. Together, these results suggest that confinement due to fibrosis may cause more deleterious effects on normal tissue compared to tumors.

Our 3D low yield stress microgel platform revealed a possible strategy by which organoids coordinate an active and collective pulsing behavior to respond to confinement. We demonstrated that tumor organoids displaced adjacent microgels along linear displacement tracks oriented in the direction of organoid expansion. In contrast, normal

organoids pulsed rarely if at all, rather exhibiting rotational behaviors consistent with Tan et al40. We demonstrated that organoid rotations generate traction forces along the rotational axis, displacing adjacent microgels in a direction parallel to the organoid. Rotation was less effective than pulsing at locally yielding microgel and creating additional space for organoid expansion, suggesting that pulsing may enable tumors to overcome confinement. The extent to which collective pulsing alters the microenvironment and its consequences in vivo are exciting areas of new investigation made possible using our 3D microgel platform.

4.0 Conclusions

1. Low yield stress microgel platforms supports organoid lumenogenesis even in scarce Matrigel® microenvironments (<50 vol.%). Microgels can be used to increase packing density and tune confinement by increasing storage modulus (G'), yield stress (σ_y), and decreasing channel width.
2. Confinement (75 vol.% microgel, 25 vol.% Matrigel®) decreases normal organoid diameter and suppresses growth. Confinement does not impact tumor organoid diameter or expansion rate.
3. Confinement disrupts apicobasal polarity and columnar-to-squamous transitions in normal organoids independent of cell division.
4. Confinement increases tumor organoid pulse frequency by at least 2×, and forskolin treatment can induce pulsing in normal organoids.

5. Materials & Methods

5.01 Hydrogel Synthesis and Microgel Preparation

The "more confined" 3D microenvironment in this study was designed as a granular bed of soft aqueous microgels with Matrigel® occupying interstitial space. Previous studies have established that microgel media support the 3D culture of cells and microtissues.[58,59] Microgel media may be composed of high-water-content hydrogel-based materials, including polyethylene glycol (PEG) and polyacrylamide (PAAm).[60–65] In this investigation, polyacrylamide was selected due to its extensive use in biomedical applications, tunable mechanical properties, lubricity,[66–68] optical transparency, and ease of preparation and accessibility (e.g., SDS-PAGE gels). Hydrogels constituents acrylamide (AAm), N,N′-methylene- bis(acrylamide) (MBAm), N,N,N′,N′-tetramethylethylenediamine (TEMED), and ammonium persulfate (APS) were purchased from Sigma-Aldrich. Stock solutions of AAm (30 wt.%), MBAm (2 wt.%), TEMED (10 vol.%, corresponding to 7.9 wt.%), and APS (10 wt.%) were prepared in ultrapure deionized (DI) water (18.2 MΩ·cm). Polyacrylamide hydrogels were synthesized at 3 wt.% AAm with a crosslinker concentration of 0.12 wt.% MBAm. Bulk hydrogels were mechanically processed and sorted by Stokes' sedimentation following the methods described in Atkins et al.59 to achieve an average microgel diameter of 104 ± 17 μm S.D. (Supplementary Materials 1). Microgels were imaged using a Nikon Ti2 Widefield Microscope with a Plan Fluor 4× (NA = 0.13) air objective and an S Plan Fluor 20× ELWD (NA = 0.45) air objective. Average microgel diameters were measured by defining three points at the edge of each microgel particle (n = 200) and fitting a circle that contained all three points.[69] Microgel diameters were determined using the 3-point circle fitting tool in the NIS Element software.

5.02 Fluorescent Nanoparticle-Embedded Microgels

Dilute concentrations of fluorescent nanoparticles were embedded within microgel particles to visualize the 3D structure of microgel-Matrigel® composites and to conduct

particle tracking with confocal imaging. Polyacrylamide microgels were prepared with 0.01 wt.% orange fluorescent polystyrene nanoparticles (500 nm diameter) to pre-polymerized hydrogel solutions. Fluorescent nanoparticles were purchased (Fisher Scientific cat.#R500) at a stock concentration of 1% solids with excitation and emission spectra (exc. 542 nm/em. 612 nm) and ultrasonicated to reduce agglomeration.

5.03 Generation of Confined Microenvironment using Microgel-Matrigel® Composite

Microgels equilibrated in Mouse Split Media at 4°C for at least 48 h prior to experimentation. Equilibrated microgels were centrifuged at 2,000g for 1 min then mixed at 75:25 volume ratios with Corning®Matrigel® Growth Factor Reduced Basement Membrane Matrix, Phenol Red-free, LDEV-free (Corning®, cat.#356231) with a protein content between 8 and 9.5 mg/mL to support the continuous culture of murine tissue-derived pancreas ductal organoids. Fluorescent FITC-Matrigel® was prepared by adding 2.5 mg/mL FITC (ThermoFisher Scientific, cat.#46424) to chilled Matrigel® for a final FITC concentration of 100 μM. FITC-Matrigel® was incubated for 30 min on ice before incorporation in microgel composites. Microgel-Matrigel® composites (75 vol.% microgel, 25 vol.% Matrigel®) equilibrated for 10 min at 37°C, 5% CO2, and 88% RH followed by two rounds of 1x Dulbecco's Phosphate Buffered Saline (DPBS) (Gibco, cat.#14040117) washes.

5.04 Matrigel® Channel Width Measurements

FITC-Matrigel® was mixed with nanoparticle-embedded microgels at 50 vol.% microgel or 75 vol.% microgel and equilibrated at 37°C for at least 10 min prior to imaging. Confocal imaging was conducted using a Nikon A1R Laser Scanning Confocal Microscope with a PlanAPO lambda 10× air objective (NA: 0.45), 1 AU pinhole, 2.2 μm step size, and 156 μm in the z-dimension (71 z-slices). Matrigel® channel widths were determined for the 50 vol.% and 75 vol.% microgel composites using the built-in,

calibrated local thickness tool in FIJI (for additional details, see Supplementary Materials 3A, B).

5.05 Rheological Characterization of Engineered Microenvironments

Rheological properties of pure Matrigel® ("less confined") and microgel-Matrigel® composites ("more confined") were measured using a TA Instruments® ARES G2 strain-controlled rotational rheometer. All rheological testing used stainless steel parallel plate upper geometry (25 mm diameter), Advanced Peltier Stage (APS) standard flat plate (TA Instruments®, cat.#402619.901) lower geometry, and constant geometry gap of 400 μm. Sample temperature was maintained at 37°C in a humidified (≈88% RH) and enclosed solvent trap for all experiments. Matrigel® gelation time was maintained at 300 s for all samples prior to experimentation, beyond the gelation time reported by Corning® (☐ 250 s). Average storage moduli (G') were determined in the linear viscoelastic region (0.1 to 1% oscillatory strain) for each sample during amplitude sweeps conducted at a frequency f = 1 Hz (Supplementary Figures 2, 3). Average yield stresses, σ_y, were calculated at the crossover point of storage and loss moduli intersect (G′ = G′′) and determined using a linear and cubic spline combination (Cubic/Linear (Orche) method in the Trios software that has been well described in rheological studies.[70,71]

5.06 Murine Tissue-Derived Pancreas Ductal Organoids

Three healthy wildtype organoid lines (mN10, mN11, and mN12) and three primary tumor Kras+/LSL-G12D; Trp53+/LSL-R172H; Pdx1-Cre ("KPC") organoid lines (mT8, mT9, and mT69A) were independently generated and generously gifted by the Tuveson Lab (Cold Spring Harbor Laboratory).[12] Pancreas ductal organoids were maintained in Matrigel®-dome culture up to passage 40 in GenClone® tissue culture treated, 24-well, flat-bottom polystyrene plates (Genesee Scientific, cat.#25-107). Organoid media formulations are detailed below and adapted from Boj et al.[12]

For R-Spondin conditioned media production, HEK 293T-HA-Rspo1-Fc cells (Trevigen cat.# 3710-001-K) were thawed in Dubecco's Modified Eagle Medium/Ham's F-12, high glucose, 110 mg/L sodium pyruvate (Gibco cat.#12-634-010) supplemented with penicillin/streptomycin (1%, Gibco, cat.#15-140-122) and heat inactivated fetal bovine serum (10%, Sigma, cat.#4135). Cells were expanded to six 182 cm^2 tissue culture flasks (Fischerbrand, cat.#FB012939) and selected using 300 µg/mL Zeocin selection reagent (Gibco, cat.#R25001). When 80-90% confluent, the cells were washed twice with DPBS, the culturing medium was changed to Mouse Split Medium, and the cells were allowed to grow for 10 days. The conditioned media was then carefully collected, centrifuged at 300g for 5 min to remove debris, and pooled and filtered through a 0.2 µM filter into a sterile bottle (Fisherbrand, cat.#FB12566504). The conditioned media was kept at 4°C for up to four months.

Mouse Split Media was used to resuspend organoids encapsulated in Matrigel® during passaging and plating. Mouse Split Media is Dubecco's Modified Eagle Medium/Ham's F-12, high glucose, 110 mg/L sodium pyruvate (Gibco, cat.#12-634-010) supplemented with 1% each of GlutaMAXTM 100□ (Gibco, cat.#35-050-061), penicillin/streptomycin (Gibco, cat.#15-140-122), and HEPES 1M (Gibco, cat.#15-630-080). Organoids were grown in Matrigel® domes overlaid with Mouse Complete Feed Media. Mouse Complete Feed Media is Mouse Split Media supplemented with: A83-01 (0.21 µg/mL, TOCRIS, cat.#29-391-0), EGF recombinant mouse protein (0.05 µg/mL, Gibco, cat.#PMG8041), recombinant human FGF-10 (0.1 µg/mL, Peprotech cat.#100-26), Gastrin I (0.021µg/mL, TOCRIS, cat.#30-061), mouse Noggin recombinant protein (0.1 µg/mL, Peprotech, cat.#250-38), N-acetylcysteine (0.2 mg/mL, Sigma-Aldrich, cat.#A9165), Nicotinamide (1.22 mg/mL, Sigma-Aldrich, cat.#N0636), B27 serum-free supplement 50□ (2%, Gibco, cat.#17-504-044), and R-Spondin1-conditioned medium

(10%, see R-Spondin1 Media Production section next). When thawing organoids, Mouse Complete Feed Media was supplemented with Y-27632 hydrochloride (3.6 mg/mL, Cayman Chemical, cat.#10005583) for the first passage only.

5.07 Extended Live DIC Imaging

Organoids cultured in Matrigel® ("less confined") or microgel composites ("more confined") were plated in Ibidi µ-Slide 8 Well plates with a #1.5 cover glass bottom (Idibi, cat. #80827) and maintained in 5% CO2, 88% RH, and 37°C conditions for 15 min before overlaying with pre-warmed Mouse Complete Feed Media. Organoids were imaged using a Leica DMi8 widefield microscope with either a HC PL FLUOTAR 10× (NA = 0.30) or HC PL FLUOTAR L 20× Ph1 (NA = 0.40) objective at 5% CO2, 88% RH, and 37°C. Z-stacks were collected every 15 min for 48 h and spanned approximately 200 µm in z with a z-step of 20 µm. Organoid expansion movies were generated by manual identification of each organoid's widest equatorial plane at each timepoint to create final single plane movies (Supplementary Movies 1-4). We developed a semi-automated method for organoid area segmentation using built-in FIJI edge detection. Movies were segmented and converted to binary objects to determine area change over time. For movies where multiple organoids were in frame or edge detection did not provide high fidelity segmentation over 48 h, manual segmentation was performed by drawing organoid regions of interest over every time frame. Area data was analyzed and plotted using GraphPad Prism version 10.1.1 for Mac, GraphPad Software, Boston, Massachusetts USA, www.graphpad.com.

5.08 Immunofluorescence

Organoids were cultured for 48 h in glass bottom well plates in either "less confined" or "more confined" conditions prior to fixation. All wash steps were allowed to

incubate for 10 min at room temperature and were performed three times unless otherwise stated. Samples were first washed once with DPBS, then fixed in 2 vol.% paraformaldehyde (16% stock, Electron Microscopy Sciences, cat.# 15710) diluted in DPBS at room temperature for 20 min. Samples were then washed with PBS +0.75% Glycine (PBS-G). Samples were then washed with Immunofluorescence Wash Buffer (IFWB). IFWB was prepared at 10× and consists of PBS + 2.5g NaN3, 5.0g Bovine Serum Albumin (Fraction V) (Sigma Aldrich, cat.#A3059), 10 mL Triton X-100 (Sigma Aldrich, cat.# T8787), and 2.5 mL Tween-20 (Sigma Aldrich, cat.# P1379). IFWB was diluted to 1□ in DI water. Samples were then incubated in IFWB containing 10 vol.% goat serum (Sigma Aldrich, cat.#G9023) (blocking buffer) for 1 h at room temperature, then stained with primary antibodies diluted in blocking buffer at 4°C overnight. Samples were then washed with IFWB, and then stained with secondary antibodies diluted in blocking buffer for 1 h at room temperature in the dark. Samples were then washed with IFWB and mounted using Vectashield anti-fade mounting medium (Vector Laboratories, cat.#H-1000).

5.09 Organoid Lumen Size Measurements

End-point brightfield images of organoids were taken at 48 h using a Nikon Ti2 Widefield microscope with a Plan Fluor 4×PhL DL objective (NA = 0.13) at 5% CO2, 88% RH. Z-stacks spanned approximately 1.1 mm with a z-step of 20 µm. The widest region of each organoid was manually determined, and the organoid outer diameter was measured in FIJI by drawing a bisecting line across the equatorial plane of each organoid. A minimum of 300 organoids were measured per microenvironmental condition.

5.10 Single Particle Tracking Confocal Microscopy

Confocal imaging was conducted using a Nikon Confocal A1R Laser Scanning Microscope in Resonant scanning mode. Organoids were fluorescently labeled at the time of plating by incubating the organoid pellet in media solution at 1:500 InvitrogenTMCellTrackerTM CMFDA (ThermoFisher cat.#C34552) for 30 min prior to resuspension in Matrigel® ("less confined") or microgel composites ("more confined"). At 24 h, organoids with lumen were identified and imaged every 30 min for an additional 24 h. The equatorial plane of each organoid was manually determined, and maximum intensity projections were generated in FIJI from volumes spanning ±16 μm in the z-dimension centered around the organoid equatorial plane. A 100 × 100 μm ROI was drawn at the interface of the organoid membrane and adjacent microgel microparticle embedded with fluorescent nanoparticles (see Section 8.02). Nanoparticle displacement trajectories indicating organoid-induced microgel movements were determined using the Mosaic FIJI plugin. To account for nanoparticles moving in and out of the focal plane, trajectories that persisted for less than 5 h were excluded from analysis.

5.11 Organoid Inflation Assay

Organoids in pure Matrigel® ("less confined") or in microgel composite ("more confined") were plated in CellVis 96-Well Glass Bottom Plates with a #1.5 cover glass bottom (CellVis, cat.#P96-1.5H-N), overlaid with pre-warmed Mouse Complete Feed Media, and returned to 5% CO2, 88% RH, and 37°C conditions for 24 h. After 24 h, organoids were treated with either dimethyl sulfoxide (SigmaAldrich, cat.# S-002-D, 20.5 mM) para-amino Blebbistatin (Cayman Chemicals, cat.#22699, 10 μM), Y-27637 Hydrochloride (Cayman Chemicals, cat.#1000583, 10.5 μM), Cytochalasin B (SigmaAldrich, cat.#C2743, 5 μM), CFTR(inh)-172 (MedChem Express, cat.#HY-16671, 10 μM), MRTX-1133 (MedChem Express, cat.#HY-134813, 5 μM), Wortmannin (SigmaAldrich, cat.#19545-26-7, 1 μM), Forskolin (MechChem Express, cat.#HY-15371,

5 μM), ETH-1864 (Cayman Chemicals, cat.#17258, 20 μM), or VX-11e (Selleckchem, cat.#S7709, 10 μM). Organoids were imaged using a Leica DMi8 widefield microscope with an HC PL FLUOTAR 10× (NA = 0.30) objective at 5% CO2, 88% RH, and 37°C. Z-stacks were collected every 30 min for 24 h and spanned 600 – 800 μm in z with a z-step of 25 μm. Each field of view was analyzed for the percent of organoids in view that exhibited □□ 1 pulse over 24 h. Organoids were scored as either pulsing or non-pulsing with a minimum of 7 organoids averaged per field of view.

5.12 Statistical Analysis

All statistical analyses were performed using GraphPad Prism version 10.1.1 for Mac, GraphPad Software, Boston, Massachusetts USA, www.graphpad.com.

References

1. Stowers, R. S. et al. Matrix stiffness induces a tumorigenic phenotype in mammary epithelium through changes in chromatin accessibility. Nat. Biomed. Eng. 3, 1009–1019 (2019).

2. Stowers, R. S. et al. Extracellular Matrix Stiffening Induces a Malignant Phenotypic Transition in Breast Epithelial Cells. Cell. Mol. Bioeng. 10, 114–123 (2017).

3. Provenzano, P. P. et al. Collagen reorganization at the tumor-stromal interface facilitates local invasion. {BMC} Med. 4, 38 (2006).

4. Papalazarou, V. et al. Collagen VI expression is negatively mechanosensitive in pancreatic cancer cells and supports the metastatic niche. J. Cell Sci. 135, (2022).

5. Huang, W. et al. Pattern of invasion in human pancreatic cancer organoids is associated with loss of SMAD4 and clinical outcome. 80, 2804–2817 (2021).

6. Abrego, J. et al. A Cancer Cell–Intrinsic GOT2–PPARδ Axis Suppresses Antitumor Immunity. Cancer Discov. 12, 2414–2433 (2022).

7. Xiao, W. et al. Matrix stiffness mediates pancreatic cancer chemoresistance through induction of exosome hypersecretion in a cancer associated fibroblasts-tumor organoid biomimetic model. Matrix Biol. Plus 14, 100111 (2022).

8. Mello, A. M. et al. Hypoxia promotes an inflammatory phenotype of fibroblasts in pancreatic cancer. Oncogenesis 11, 56 (2022).

9. Rice, A. J. et al. Matrix stiffness induces epithelial–mesenchymal transition and promotes chemoresistance in pancreatic cancer cells. Oncogenesis 6, e352–e352 (2017).

10. Helms, E. J. et al. Mesenchymal Lineage Heterogeneity Underlies Nonredundant Functions of Pancreatic Cancer–Associated Fibroblasts. Cancer Discov. 12, 484–501 (2022).

11. Olivares, O. et al. Collagen-derived proline promotes pancreatic ductal adenocarcinoma cell survival under nutrient limited conditions. Nat. Commun. 8, 16031 (2017).

12. Boj, S. F. et al. Organoid Models of Human and Mouse Ductal Pancreatic Cancer. Cell 160, 324–338 (2015).

13. Grünwald, B. T. et al. Spatially confined sub-tumor microenvironments in pancreatic cancer. Cell 184, 5577-5592.e18 (2021).

14. Barbazan, J. et al. Cancer-associated fibroblasts actively compress cancer cells and modulate mechanotransduction. Nat. Commun. 14, 6966 (2023).

15. Maurer, C. et al. Experimental microdissection enables functional harmonisation of pancreatic cancer subtypes. Gut 68, 1034–1043 (2019).

16. Jeong, Y. J. et al. Morphology-guided transcriptomic analysis of human pancreatic cancer organoids reveals microenvironmental signals that enhance invasion. J. Clin. Invest. 133, (2023).

17. Hsia, C.-R. et al. Confined migration induces heterochromatin formation and alters chromatin accessibility. iScience 25, 104978 (2022).

18. Bell, E. S. et al. Low lamin A levels enhance confined cell migration and metastatic capacity in breast cancer. Oncogene 41, 4211–4230 (2022).

19. Jiang, K., Liang, L. & Lim, C. T. Engineering confining microenvironment for studying cancer metastasis. iScience 24, 102098 (2021).

20. Heo, S.-J. et al. Nuclear softening expedites interstitial cell migration in fibrous networks and dense connective tissues. Sci. Adv. 6, (2020).

21. Fanfone, D. et al. Confined migration promotes cancer metastasis through resistance to anoikis and increased invasiveness. Elife 11, (2022).

22. Palamidessi, A. et al. Unjamming overcomes kinetic and proliferation arrest in terminally differentiated cells and promotes collective motility of carcinoma. Nat. Mater. 18, 1252–1263 (2019).

23. Nader, G. P. de F. et al. Compromised nuclear envelope integrity drives {TREX1}-dependent {DNA} damage and tumor cell invasion. Cell 184, 5230-5246.e22 (2021).

24. Chang, J. et al. Cell volume expansion and local contractility drive collective invasion of the basement membrane in breast cancer. Nat. Mater. (2023) doi:10.1038/s41563-023-01716-9.

25. Hof, L. et al. Long-term live imaging and multiscale analysis identify heterogeneity and core principles of epithelial organoid morphogenesis. BMC Biol. 19, 37 (2021).

26. Tiriac, H., Plenker, D., Baker, L. A. & Tuveson, D. A. Organoid models for translational pancreatic cancer research. Curr. Opin. Genet. Dev. 54, 7–11 (2019).

27. Baker, L. A., Tiriac, H., Clevers, H. & Tuveson, D. A. Modeling Pancreatic Cancer with Organoids. Trends in Cancer 2, 176–190 (2016).

28. Tiriac, H. et al. Organoid Profiling Identifies Common Responders to Chemotherapy in Pancreatic Cancer. Cancer Discov. 8, 1112–1129 (2018).

29. Huch, M. et al. Long-term culture of genome-stable bipotent stem cells from adult human liver. Cell 160, 299–312 (2015).

30. Graham, A. J. et al. MAGIC matrices: freeform bioprinting materials to support complex and reproducible organoid morphogenesis. bioRxiv 2024.02.01.578324 (2024).

31. Dudaryeva, O. Y. et al. {3D} confinement regulates cell life and death. Adv. Funct. Mater. 2104098 (2021) doi:10.1002/adfm.202104098.

32. Popkova, A., Rauzi, M. & Wang, X. Cellular and Supracellular Planar Polarity: A Multiscale Cue to Elongate the Drosophila Egg Chamber. Front. Cell Dev. Biol. 9, (2021).

33. Trushko, A. et al. Buckling of an Epithelium Growing under Spherical Confinement. Dev. Cell 54, 655-668.e6 (2020).

34. Sumbal, J., Fre, S. & Sumbalova Koledova, Z. Fibroblast-induced mammary epithelial branching depends on fibroblast contractility. {PLoS} Biol. 22, e3002093 (2024).

35. Paksa, A. et al. Repulsive cues combined with physical barriers and cell-cell adhesion determine progenitor cell positioning during organogenesis. Nat. Commun. 7, 11288 (2016).

36. Barbazán, J. & Matic Vignjevic, D. Cancer associated fibroblasts: is the force the path to the dark side? Curr. Opin. Cell Biol. 56, 71–79 (2019).

37. Bhattacharjee, S. et al. Tumor restriction by type I collagen opposes tumor-promoting effects of cancer-associated fibroblasts. J. Clin. Invest. (2021).

38. Wisdom, K. M. et al. Covalent cross-linking of basement membrane-like matrices physically restricts invasive protrusions in breast cancer cells. Matrix Biol. 85–86, 94–111 (2020).

39. Navis, A. & Nelson, C. M. Pulling together: Tissue-generated forces that drive lumen morphogenesis. Semin. Cell Dev. Biol. 55, 139–147 (2016).

40. Molnár, R. et al. Mouse pancreatic ductal organoid culture as a relevant model to study exocrine pancreatic ion secretion. Lab. Investig. 100, 84–97 (2020).

41. Tan, T. H. et al. Emergent chirality in active solid rotation of pancreas spheres. bioRxiv (2022) doi:10.1101/2022.09.29.510101.

42. Boj, S. F. et al. Forskolin-induced Swelling in Intestinal Organoids: An In Vitro Assay for Assessing Drug Response in Cystic Fibrosis Patients. J. Vis. Exp. (2017) doi:10.3791/55159.

43. Tallapragada, N. P. et al. Inflation-collapse dynamics drive patterning and morphogenesis in intestinal organoids. Cell Stem Cell 28, 1516-1532.e14 (2021).

44. Chugh, M., Munjal, A. & Megason, S. G. Hydrostatic pressure as a driver of cell and tissue morphogenesis. Semin. Cell Dev. Biol. 131, 134–145 (2022).

45. Stylianopoulos, T. et al. Causes, consequences, and remedies for growth-induced solid stress in murine and human tumors. Proc. Natl. Acad. Sci. 109, 15101–15108 (2012).

46. So, W. Y. et al. YAP localization mediates mechanical adaptation of human cancer cells during extravasation in vivo. bioRxiv (2023) doi:10.1101/2023.11.14.567015.

47. Lee, J. Y. et al. YAP-independent mechanotransduction drives breast cancer progression. Nat. Commun. 10, 1–9 (2019).

48. Padera, T. P. et al. Cancer cells compress intratumour vessels. Nature 427, 695–695 (2004).

49. Gómez-Gálvez, P. et al. Scutoids are a geometrical solution to three-dimensional packing of epithelia. Nat. Commun. 9, 2960 (2018).

50. Lemke, S. B. & Nelson, C. M. Dynamic changes in epithelial cell packing during tissue morphogenesis. Curr. Biol. 31, R1098–R1110 (2021).

51. Paré, A. C. et al. A positional Toll receptor code directs convergent extension in Drosophila. Nature 515, 523–527 (2014).

52. Langthasa, J. et al. Extracellular matrix mediates moruloid-blastuloid morphodynamics in malignant ovarian spheroids. Life Sci. Alliance 4, e202000942 (2021).

53. Chan, C. J. et al. Hydraulic control of mammalian embryo size and cell fate. Nature 571, 112–116 (2019).

54. Itoi, F. et al. Offspring from Mouse Embryos Developed Using a Simple Incubator-Free Culture System with a Deoxidizing Agent. PLoS One 7, e47512 (2012).

55. Mosaliganti, K. R. et al. Size control of the inner ear via hydraulic feedback. Elife 8, (2019).

56. Schnipper, J., Dhennin-Duthille, I., Ahidouch, A. & Ouadid-Ahidouch, H. Ion Channel Signature in Healthy Pancreas and Pancreatic Ductal Adenocarcinoma. Front. Pharmacol. 11, (2020).

57. Hofschröer, V. et al. Ion Channels Orchestrate Pancreatic Ductal Adenocarcinoma Progression and Therapy. Front. Pharmacol. 11, (2021).

58. Nguyen, D. T. et al. 3D In Vitro Platform for Cell and Explant Culture in Liquid-like Solids. Cells 11, 967 (2022).

59. Atkins, D. J. et al. Survival-Associated Cellular Response Maintained in Pancreatic Ductal Adenocarcinoma (PDAC) Switched Between Soft and Stiff 3D Microgel Culture. ACS Biomater. Sci. Eng. 10, 2177–2187 (2024).

60. Bhattacharjee, T. et al. Writing in the granular gel medium. Sci. Adv. 1, 4–10 (2015).

61. Muir, V. G., Prendergast, M. E. & Burdick, J. A. Fragmenting Bulk Hydrogels and Processing into Granular Hydrogels for Biomedical Applications. J. Vis. Exp. (2022) doi:10.3791/63867.

62. O'Bryan, C. S. et al. Three-dimensional printing with sacrificial materials for soft matter manufacturing. MRS Bull. 42, 571–577 (2017).

63. Bhattacharjee, T. et al. Polyelectrolyte scaling laws for microgel yielding near jamming. Soft Matter 14, 1559–1570 (2018).

64. Bhattacharjee, T. et al. Liquid-like Solids Support Cells in 3D. ACS Biomater. Sci. Eng. 2, 1787–1795 (2016).

65. LeBlanc, K. J. et al. Stability of High Speed 3D Printing in Liquid-Like Solids. ACS Biomater. Sci. Eng. 2, 1796–1799 (2016).

66. Urueña, J. M. et al. Mesh Size Control of Polymer Fluctuation Lubrication in Gemini Hydrogels. Biotribology 1–2, 24–29 (2015).

67. Chau, A. L. et al. pH-Dependent Friction of Polyacrylamide Hydrogels. Tribol. Lett. 71, 108 (2023).

68. Chau, A. L., Edwards, C. E. R., Helgeson, M. E. & Pitenis, A. A. Designing Superlubricious Hydrogels from Spontaneous Peroxidation Gradients. ACS Appl. Mater. Interfaces 15, 43075–43086 (2023).

69. Garcia-Lopez, J. & Ramos, P. A. Fitting a Set of Points by a Circle. Proc. Thirteen. Annu. Symp. Cumputational Geom. (1997).

70. Zhang, R. & Schweizer, K. S. Theory of nonlinear elasticity, stress-induced relaxation, and dynamic yielding in dense fluids of hard nonspherical colloids. J. Chem. Phys. 136, (2012).

71. Ghosh, A. et al. Linear and nonlinear rheology and structural relaxation in dense glassy and jammed soft repulsive pNIPAM microgel suspensions. Soft Matter 15, 1038–1052 (2019).

Chapter 4: Concluding Remarks and Perspectives

This dissertation focused a central theme–the material properties of the extracellular microenvironment can both support and disrupt healthy tissue biology. My investigations implemented granular, polyacrylamide microgels to extend the imaging lifetime of zebrafish embryonic development and investigate the biomechanics in tissue-derive, pancreas ductal organoids from healthy and tumor origins.

Herein, I identified the narrow range material properties supportive of zebrafish morphogenesis by rigorously characterizing the rheological and optical properties of a suite of low polymer concentration microgels. These findings demonstrated the importance of microenvironmental mechanics in supporting and disrupting zebrafish morphogenesis while addressing a limitation in the zebrafish field—how to image embryonic development over long timescales (>24 h) while minimizing drift in the z-dimension and without constraining morphogenesis. More broadly, these findings underscore the importance of microenvironmental rheology in directing process from the cellular to the organism scale. This work further identifies the rheology of the experimental embedding medium as consequential for observing biological processes. I believe there is an opportunity for fields across developmental biology to optimize the rheology of embedding mediums to minimize disruptions to morphogenesis.

These works concluded by investigating the role of microenvironmental mechanics on PDAC organoids. I developed a microgel composite system that confined organoid expansion by increasing both the stiffness and yield stress of the microenvironment. I observed PDAC organoids not only grew more effectively in composite microenvironments but also exhibited an emergent pulsing behavior that

was accelerated when confined. Tunable, 3D microgel composites provided a platform to create a "fibrotic" microenvironment *in* vitro and revealed how confinement negatively affects normal organoid growth while leaving tumor organoids unaffected. Our mechanistic studies demonstrated confinement disrupts native apicobasal polarity and implicated hydrostatic pressure regulation as a key determinant of organoid pulsing and likely expansion in microgel composites. Cryptic epithelia utilize several pressure regulation mechanisms to prevent excessive pressure buildup in a central lumen, and our observations suggest that normal and tumor organoids utilize distinct regulatory mechanisms whereby normal organoids relieve lumen pressure while tumor organoids build up pressure. A better understanding of pressure regulation in organoid models is essential for deepening our knowledge of interstitial pressure increases found *in vivo* during PDAC disease transition.

These works established an important role of the confining, spatial features of the tumor microenvironment in disease biology. The fibrotic tumor environment plays a central role in aiding tumor outgrowth by impairing immune cell infiltration and providing nutrients for cancer cells to scavenge. The highly fibrotic tumor microenvironment exerts compressive stresses on healthy and cancer cells which, based on our observations, likely has more deleterious effects on healthy tissue over tumors. Key questions that arise from this study include:

1) how do tumor organoids establish higher pressure lumen, and is this regulated at a cytoskeletal, ion transport, or cell junction level?

2) how is polarity regulated by the mechanical microenvironment, and what mechanosensory proteins interact with the polarity complexes?

3) how does confinement alter immune cell and fibroblast function?

These areas of exploration are exciting opportunities to merge immunology, cell biology, and materials engineering to better model the dynamics of the tumor microenvironment *in vitro*.